Studies of Intrinsic Localized Modes in a Nonlinear Electric Lattice with Saturable Nonlinearity

Weihua Shi

July 2014

Dissertation

Studies of Intrinsic Localized Modes in a Nonlinear Electric Lattice with Saturable Nonlinearity

Graduate School of Natural Science and Technology, Kanazawa University

Division of Mathematical and Physical Sciences

Laboratory of Nonlinear Physics

Student ID Number 1123102009

Name Weihua Shi

Advisor Masayuki Sato

Abstract

In this work experimental observations of step-widening (-narrowing) intrinsic localized mode (ILM) have been achieved in the nonlinear electric lattice by using MOS-capacitors with saturable nonlinearity. These follow the theoretical work of Hadžievski and coworkers who have demonstrated that in the discrete nonlinear Schrödinger (DNLS) lattices with saturable nonlinearity ILM alternates between site-centered and bond-centered locations when Peierls-Nabarro (PN) barrier changes its sign.

It has been observed experimentally that the ILM switches above two shapes alternatively at the step-widening transitions. Linear response spectrum measurement provides a way to explore mechanisms of transitions, through peak shifts of natural frequency (NF) of the ILM as well as the linear local mode (LLM) produced by the ILM. It indicates that step transitions are attributed to the softening of the 1st-LLM frequency difference which corresponds to the decreasing of the PN barrier height.

In addition, by the linear response spectra the lower fundamental transition observed at the lower edge of the stable ILM region is similar to the saddle-node bifurcation in the Duffing resonator and it is due to the softening of NF. The linear response spectra also reveal creation of new LLM at each step of the ILM width increment.

These findings are supported by numerical simulations. A model we used is based on the nonlinear lattice as the same as in experiments. The simulation results show a good agreement with experimental works.

Different from the theoretical work, we observed a hysteresis at step transitions. This hysteresis prevents a free traveling. However, we have succeeded decreasing the

hysteresis by tuning the lattice. If the hysteresis becomes negligibly small, the ILM runs freely.

Acknowledgements

I am heartily thankful to my advisor, Prof. Masayuki Sato, whose encouragement, guidance and support enabled me to develop an understanding of the subject. I would like to thank Prof. Koichi Matumoto and Lecture Satoshi Abe for lending me the distilled water maker. I would also like to thank Mr.Nunomura for supplying the liquid helium.

I would like to thank Shoma Shige for helping with my experiments as well as improving my knowledge about Japanese culture. I would also like to thank Yuichi Takao for helping me to finish my experiment. Thanks also to Tatsuya Ishikawa and Tahiro Nakaguchi for helping me collect electronic elements. Best wishes to Hiroaki Hasebe who is busying in job-hunting. I also thank Jianbo Lin for giving some advice in LATEX,

Lastly, I offer my regards and blessings to all of those who supported me in any respect during the completion of the project.

Contents

Abstract **i**

Acknowledgements **iii**

List of Tables **vi**

List of Figures **vii**

1 Introduction **1**

1.1 Background information 1

1.2 Organization of Thesis 4

2 Reviews **10**

2.1 The stability of nonlinear localized mode in lattices with saturable nonlinearity [1] 10

2.2 The natural frequency (NF) of the ILM [2] 12

3 Experimental measurements **18**

3.1 The nonlinear electrical lattice containing MOS-capacitor 18

3.2 Experimental results: variable width ILM 23

4 Numerical simulations **32**

4.1 The model of simulation 32

4.2 Simulated results 35

5 Discussions **43**

5.1 Stepwise varying width of the ILM. 43

5.2 The NF and other LLMs 48

5.3 The hysteresis inside the stable ILM region 50

6 Summary **57**

List of Tables

List of Figures

2.1 PN potential versus power P 11

2.2 Power dependence of amplitude 11

2.3 Experimentally observed AR amplitude in MEMS 14

2.4 Experimental response spectra in MEMS 16

3.1 Nonlinear electrical lattice 19

3.2 C-V curves of three connections in experiments 20

3.3 Linear dispersion curve 22

3.4 Experimental voltage plots: variable width ILM 25

3.5 Linear response measurement for experiments 27

3.6 Experimental imaginary part of the linear response 28

3.7 Frequency difference of linear modes in experiments 29

4.1 Experimental and simulated C-V curves 34

4.1 Simulation results: variable width ILM 37

4.2 Simulated imaginary part of the linear response 39

4.3 Frequency difference of linear modes in simulations 41

5.1 Amplitude plot: adapted from Fig. 2 of Ref. [1] 44

5.2 Experimental vibration shapes of linear modes 46
5.3 Simulated vibration shapes of linear modes 47
5.4 Enlargements of the ILM and 1st-LLM shapes 48
5.5 Maximum amplitude: comparing hysteresis in experiments and simulations 52
5.6 Experimental voltage plots: drain open 54

Chapter 1

Introduction

1.1 Background information

In a perfect lattice system consisting of discrete elements with nonlinear interaction, time-periodic, spatially localized vibration modes can be excited. Such localized excitations are called intrinsic localized modes (ILMs) [1] that they can occur in a lattice of any dimensions. They are also referred to discrete breathers (DBs) [2] or lattice solitons [3] with considering as the discrete analogues of solitions in continuous matter. As the localized modes of defects in a harmonic lattice, for a system with hard nonlinearity, ILMs jump up from the dispersion curve maximum, whereas for soft nonlinearity they fall out of the dispersion minimum.

Since the first report by Sievers and Takeno [1] in the late 1980s, ILMs have been studied extensively in various fields in physics. The prediction that ILMs may occur in ideal anharmonic lattices [1, 4] had been verified with computer simulation in one-dimensional and two-dimensional lattices [5]. Because of the discreteness of atomic

arrangement and the nonlinearity of interatomic interaction, the atomic system was used widely to investigate ILMs. [6–9] Some of the efforts also devoted to studying magnetic ILMs in ferromagnetic chains. Differing from solitons, ILMs collided inelastically and transferred their energy. [10]

There is a large amount of experimental and related theoretical work on applying the ILMs concept to many different branches in physics. Experiments have demonstrated ILMs in systems as diverse as Josephson junction arrays [11, 12], antiferromagnetic structures [13], driven micromechanical cantilever arrays [14], and optical waveguide arrays [15]. Recently, ILMs also had been observed in three-dimensional crystals in thermal equilibrium; in a simple ionic crystal, NaI, above 555 K. [16] A good review of many applications of ILMs is found in Ref. [17].

As a cousin of ILMs, a nonlinear localized excitation called a soliton has a longer history. The first documented observation of the soliton phenomanon was made in August 1834 by John Scott Russell who saw a solitary water wave in the Union Canal linking Edinburgh with Glasgow in Scotland. Soltions are localized within a region and they can travel in a lattice with permanent form and velocity. Moreover, solitons can cross each other without change except for a phase shift. With these important properties, solitons have been investigated intensively in various fields: optical fibers [18, 19], biology [20–22], magnets [23] and so on. In mathematics, the difference between soliton and ILM is that the former is integrable while the latter is nonintegrable in nonlinear partial differential equations. In physics, the lattice discreteness, ignoring in soliton theory, must be taken account because ILMs are localized to small regions comparable to the lattice spacing.

The effects of discreteness on nonlinear localized modes have been analyzed by

Kivshar et al. in a lattice discrete nonlinear Schrödinger (DNLS) models. [24] They have demonstrated that the discreteness effects on nonlinear localized modes give rise to an effective periodic potential similar to the Pieierls-Nabarro (PN) potential for kink in the Frenkel-Kontorova (FK) model [25]. They also have shown that the PN potential vanishes in the intergrable Ablowitz-Ladik variant of the NLS equation while arises from the nonintegrability of the discrete models. [24] The PN potential is the barrier between the site-centered and bond-centered lattice positions of the nonlinear localized excitation that inhibits translation.

Because of the PN barrier, usually, ILMs cannot move freely in a nonlinear lattice with discreteness. Such stationary ILMs have been studied in detail in micro-electro-mechanical systems (MEMS). [26–30] The stable ILM is generated by compensating a damping by an energy feeding driver, at where the ILM is phase locked to the driver as an auto-resonant (AR) state. [31–34] Bifurcations happen at edges of stable ILM frequency region are studied by utilizing a linear response spectroscopy. [35] Sato et al. have demonstrated that both two bifurcation points are attributed to the natural frequency (NF) of the ILM, while with different mechanisms. The NF is a free oscillation that it is a linear combination of the solutions of the homogeneous equation. [36]

The topic of free traveling versus the PN barrier is of central interest, since ILMs are not restricted to motion in 1D so the control of the PN potential for an ILM would open a new avenue. In this direction a saturable nonlinearity in a DNLS equation has been proposed by Hadžievski et al. [37]. They showed that the magnitude of the PN potential as a function of energy oscillates between positive and negative values and that this alternating sign changes the stability of an ILM between the two neighboring

site centered and bond centered locations. Where the PN barrier is zero transition points exist and the ILM can move freely. (Note that DNLS is nonintegrable and therefore it supports ILMs but not lattice solitons. These localized excitations can move through the lattice with a small, but non-zero deceleration [38, 39]) Interesting properties for such a saturable nonlinearity were proposed and many theoretical follow on publications have appeared. [40–42]

Nonlinear transmission lines have been considered as one of the convenient experimental tools with which to study excitations in 1-D nonlinear lattices. [43,44] Recent experimental work has focused on ILMs [4,17] where lattice discreteness plays an important role. Such studies have ranged from manipulation of a stationary ILM [45]; to spatial control of slowly traveling ILMs [46]; to generation of ILMs by sub-harmonic driving [47]. However, there was no experimental study about the saturable nonlinearity till we demonstrated in electric lattice.

1.2 Organization of Thesis

Chapter 3 describes the experimental setups, designs and results. By employing a MOS-capacitor with saturable nonlinearity instead of a diode in the nonlinear electrical lattice, step changing of the width of the ILM have been observed. The location of the ILM alternates between site-centered and bond-centered. However an unexpected hysteresis occurs at step transitions. The mechanisms of the NF and linear localized modes (LLMs) [48] associated with the ILM have been investigated by the linear response measurement.

Chapter 4 presents numerical simulation models and the results of simulations.

The model we used in the simulation is built on the experimental nonlinear electrical lattice. [43] The results of the simulations are in agreed with the experimental results besides hysteresis that it is much smaller than in experiments.

In chapter 5, we discuss behaviors of the variable width ILM, linear modes, and hysteresis. By comparing the theoretical work [37] and measuring the vibration shapes of linear modes, we demonstrate that 1st-LLM plays an important role in step transitions. Explanations on the mechanisms of the NF and other LLMs have also been made. Finally, we describe hysteresis and show that it might be the key of the generation of moving ILMs. Chapter 6 is a summary of the main results and gives some suggestions for future work.

References

[1] A. J. Sievers and S. Takeno, *Phys. Rev. Lett.* **61**, 970-973 (1988).

[2] S. Flach and C. R. Willis, *Phys. Rep.*, **295**, 182 (1998).

[3] D. N. Christoldoulides and R. I. Joseph, *Opt. Lett.* **13**, 794 (1988).

[4] S. Takeno and A. J. Sievers, *Solid State Communications* **67**, 1023-1026 (1988).

[5] V. M. Burlakov, S. A. Kiselev, and V. N. Pyrkov, *Phys. Rev. B* **42**, 4921-4927 (1990).

[6] S. R. Bickham, A. J. Sievers, and S. Takeno, *Phys. Rev. B* **45**, 10344-10347 (1992).

[7] S. A. Kiselev, S. R. Bickham, and A. J. Sievers, *Phys. Rev. B* **48**, 13508-13511 (1993).

[8] S. R. Bickham and A. J. Sievers, *Phys. Rev. B* **43**, 2339-2346 (1991).

[9] S. Flach, K. Kladko, and C. R. Willis, *Phys. Rev. E* **50**, 2293-2303 (1994).

[10] S. V. Rakhmanova and A. V. Shchegrov, *Phys. Rev. B* **57**, R14012 (1998).

[11] E. Trias, J. J. Mazo, and T. P. Orland, *Phys. Rev. Lett.* **84**, 741-744 (2000).

[12] P. Binder, D. Abraimov, A. V. Ustinov, S. Flach, and Y. Zolotaryuk, *Phys. Rev. Lett.* **84**, 745-748 (2000).

[13] M. Sato and A. J. Sievers, *Nature* **432**, 486-488 (2004).

[14] M. Sato, B.E. Hubbard, A. J. Sievers, B. Ilic, and H.G. Craighead, *Europhys. Lett.* **66**, 318-323 (2004).

[15] H. S. Eisenberg, Y. Silberberg, R. Morandotti, A. R. Boyd, and J. S. Aitchison, *Phys. Rev. Lett.* **81**, 3383-3386(1998).

[16] M. E. Manley et al., *Phys Rev B* **79**, 134304 (2009).

[17] S. Flach, and A.V. Gorbach, *Phys. Rep.* **467**, 1-116 (2008).

[18] S. T. Cundiff, B. C. Collings, N. N. Akhmediev, J. M. Soto-Crespo, K. Bergman, and W. H. Knox, *Phys. Rev. Lett.* **82**, 3988 (1999).

[19] D. Y. Tang, H. Zhang, L. M. Zhao, and X. Wu, *Phys. Rev. Lett.* **101**, 153904 (2008).

[20] Z. Sinkala, *J. Theor. Biol.* **241**, 9191-27 (2008)

[21] T. Heimburg, and A. D. Jackson, *Biophys. Rev. Lett.* **2**, 57-78 (2007).

[22] S. S. L. Andersen, A. D. Jackson, and T. Heimburg, *Progr. Neurobiol.* **88**, 104-113 (2009).

[23] A. M. Kosevich, V. V. Gann, A. I. Zhukov, and V. P. Voronov, *Journal of Experimental and Theoretical Physics* **87**, 401-407 (1998)

[24] Y. S. Kivshar and D. K. Campbell, *Phys. Rev. E* **48**, 3077 (1993).

[25] M. Peyrard and M. D. Kruskal, *Physica D* **81**, 88 (1984).

[26] M. Sato, B. E. Hubbard, L. Q. English, B. Ilic, D. A. Czaplewski, H. G. Craighead, and A. J. Sievers, *Chaos* **13**, 702 (2003).

[27] M. Sato, B. E. Hubbard, L. Q. English, B. Ilic, D. A. Czaplewski, H. G. Craighead, and A. J. Sievers, *Phys. Rev, Lett.* **90**, 044102 (2003).

[28] M. Sato, B. E. Hubbard, and A. J. Sievers, *Rev. Mod. Phys.* **78**, 137 (2006).

[29] M. Spletzer et al., *Appl. Phys. Lett.* **89**, 254102 (2006).

[30] E. Kenig et al. *Phys. Rev. E* **80**, 046202 (2009).

[31] M. Sato et al. *Phys. Rev. Lett.* **107**, 234101 (2011).

[32] J. Fajans and L. Friedland, *Am. J. Phys.* **69**, 1096 (2001).

[33] Y. Gopher, L. Friedland, and A.G. Shagalov, *Phys. Rev. E* **72**, 036604 (2005).

[34] A. Barak et al., *Phys. Rev. Lett.* **103**, 123901 (2009).

[35] M. Sato, S. Imai, N. Fujita, W. Shi, Y. Takao, Y. Sada, B. E. Hubbard, B. Ilic, and A. J. Sievers, *Phys. Rev. E* **87**, 012920 (2013).

[36] D. W. Jordan and P. Smith, *Nonlinear Ordinary Differential Equations* (Oxford University Press, New York, 2007)

[37] L. Hadžievski, A. Maluckov, M. Stepic, and D. Kip, *Phys. Rev. Lett.* **93**, 033901 (2004).

[38] D. B. Duncan, J. C. Eilbeck, H. Feddersen, and J. A. D. Wattis, *Physica D* **68**, 1 (1993)

[39] O. F. Oxtoby and I. V. Barashenkov, *Phys. Rev. E* **76**, 036603 (2007)

[40] M. Syafwan et al., *Journal of Physics A* **45**, 075207 (2012).

[41] O. V. Borovkova, Y. V. Kartashov, and L. Torner, *Physical Review A* **81**, 063806 (2010).

[42] A. Khare et al., *Physical Review E* **74**, 016607 (2006).

[43] K. Fukushima, M. Wadati, and Y. Narahara, *J. Phys. Soc. Jpn.* **49**, 1593 (1980).

[44] B. Z. Essimbi and D. Jager, *Journal of Physics D* **39**, 390 (2006).

[45] M. Sato et al., *Europhys. Lett.* **80**, 30002 (2007).

[46] L. Q. English et al., *Phys. Rev. E* **81**, 046605 (2010).

[47] L. Q. English et al., *Phys. Rev. Lett.* **108**, 084101 (2012).

[48] V. Hizhnyakov, A. Shelkan, M. Klopov, S. A. Kiselev, and A. J. Sievers, *Phys. Rev. B* **73**, 224302 (2006).

Chapter 2

Reviews

2.1 The stability of nonlinear localized mode in lattices with saturable nonlinearity [1]

The model of this theoretical work on discrete nonlinear Schrödinger (DNLS) lattices with saturable nonlinearity has the form

$$i\frac{\partial u_n}{\partial t} + K\left(u_{n+1} + u_{n-1} - 2u_n\right) - \beta\frac{u_n}{1+|u_n|^2} = 0. \tag{2.1}$$

where K is the coupling constant, and β is the nonlinearity parameter.

Figure 2.1 shows the Peierls-Nabarro (PN) potential as a function of power P. The PN potential is defined by the energy difference between site-centered localized mode (A) and bond-centered mode (B). As the power increases, the PN potential changes its sign at the zero line. It indicates the interchange of stability between site-centered mode (A) and bond-centered mode (B) at the zero PN barrier height.

Power dependence of the amplitude for site-centered mode (A) and bond-centered

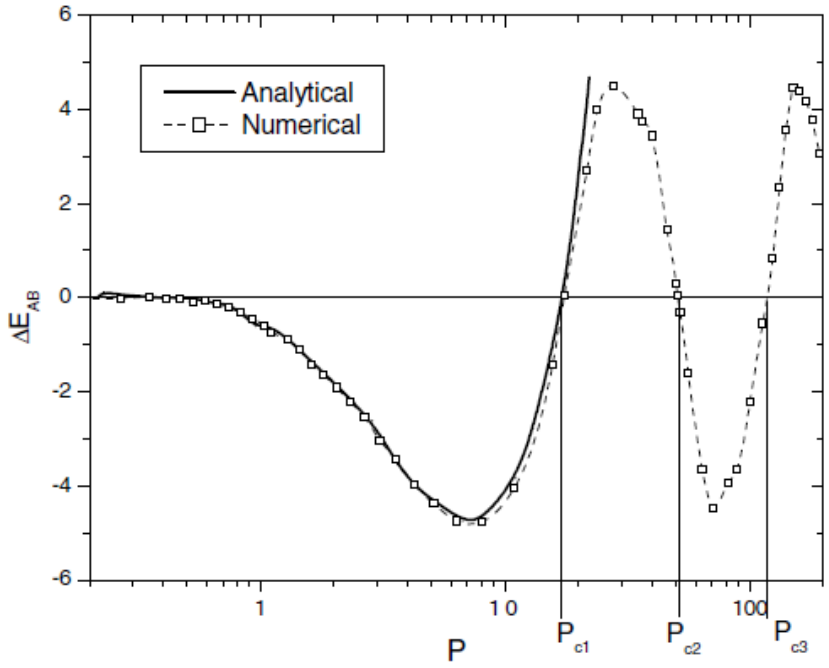

Figure 2.1: PN potential versus localized mode power P for discrete lattices. [1]. Darker is larger amplitude.

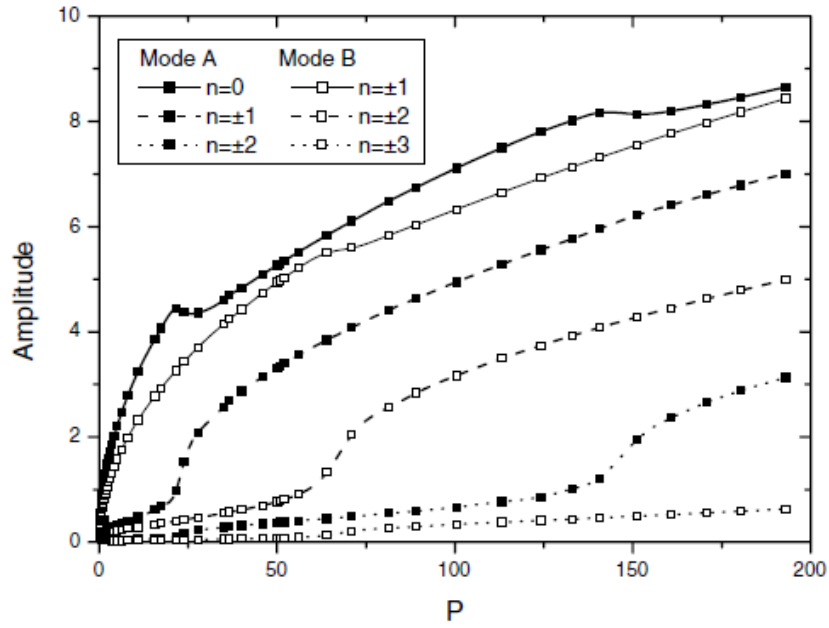

Figure 2.2: Amplitude of site-centered mode (A) and bond-centered mode (B) as a function of power P

mode (B) is presented in Fig. 2.2. Because of amplitude saturation, the site-centered mode (A) extends from $n = 0$ to $n = \pm 1$, $n = \pm 2$ as power increases. The bond centered mode (B) also has the same process. However, considering the interchange of stability between these two modes, it is clear that the stable localized mode alternates between site-centered mode (A) and bond-centered mode (B) as increasing power P.

2.2 The natural frequency (NF) of the ILM [2]

The single Duffing oscillator with weak probe is given by

$$\ddot{x} + \tfrac{1}{\tau}\dot{x} + \omega_0^2 x + \varepsilon x^3 = \alpha_d \cos(\Omega t) + \alpha_p \cos(\omega t) \tag{2.2}$$

where τ is the relaxation time, ω_0^2 is square of the linear resonance frequency, $\varepsilon > 0$ is a hard nonlinear constant, ad and ap are the acceleration amplitudes for the driver and probe. The amplitude response can be assumed by

$$x = \tfrac{1}{2}\tilde{A}e^{-i\Omega t} + \tfrac{1}{2}\tilde{a}e^{-i\omega t} + \tfrac{1}{2}\tilde{b}e^{-i\omega' t} + c.c. \tag{2.3}$$

Here ω' is the four-wave mixing frequency, $\tilde{A}$ is the large oscillation driver response, $\tilde{a}$ is the probe response, and $\tilde{b}$ is the four-component response.

Inserting Eq. 2.2 into Eq. 2.1 and retaining terms that oscillate near the driver frequency, one finds

$$\begin{aligned}
&\left(\omega_0^2 + \tfrac{3}{4}\varepsilon\left|\tilde{A}\right|^2 - \Omega^2 - i\gamma\Omega\right)\tilde{A}e^{-i\Omega t} \\
&+ \left(\omega_0^2 + \tfrac{3}{2}\varepsilon\left|\tilde{A}\right|^2 - \omega^2 - i\gamma\omega\right)\tilde{a}e^{-i\omega t} + \tfrac{3}{4}\varepsilon\tilde{A}^2\tilde{b}^* e^{-i\omega t} \\
&+ \left(\omega_0^2 + \tfrac{3}{2}\varepsilon\left|\tilde{A}\right|^2 - \omega'^2 - i\gamma\omega'\right)\tilde{b}e^{-i\omega' t} + \tfrac{3}{4}\varepsilon\tilde{A}^2\tilde{a}^* e^{-i\omega' t} \\
&= \alpha_d e^{-i\Omega t} + \alpha_p e^{-i\omega t}
\end{aligned} \tag{2.4}$$

where $\gamma = 1/\tau$. By equating each oscillating terms, the three resulting equations are

$$\left(\omega_0^2 + \tfrac{3}{4}\varepsilon\left|\tilde{A}\right|^2 - \Omega^2 - i\gamma\Omega\right)\tilde{A} = \alpha_d. \tag{2.5}$$

$$\left(\omega_0^2 + \tfrac{3}{2}\varepsilon\left|\tilde{A}\right|^2 - \omega^2 - i\gamma\omega\right)\tilde{a} + \tfrac{3}{4}\varepsilon\tilde{A}^2\tilde{b}^* = \alpha_p. \tag{2.6}$$

$$\left(\omega_0^2 + \tfrac{3}{2}\varepsilon\left|\tilde{A}\right|^2 - \omega'^2 - i\gamma\omega'\right)\tilde{b} = \tfrac{3}{4}\varepsilon\tilde{A}^2\tilde{a}^*. \tag{2.7}$$

Equation 2.5 is for the driver response. From Eqs. 2.6 and 2.7, the probe response function can be calculated as

$$\begin{aligned}\tilde{\chi}_a = \frac{\tilde{a}}{\alpha_2} &= \frac{1}{\left(\omega_{nl}^2 - \omega^2 - i\gamma\omega\right) - \frac{9}{16}\varepsilon^2\left|\tilde{A}\right|^4 \frac{1}{\left(\omega_{nl}^2 - \omega'^2 + i\gamma\omega'\right)}} \\ &= \frac{\tilde{\chi}_0(\omega)}{1 - \frac{9}{16}\varepsilon^2\left|\tilde{A}\right|^4\tilde{\chi}_0(\omega)\tilde{\chi}_0^*(\omega')}.\end{aligned} \tag{2.8}$$

where $\tilde{\chi}_0(\omega) = \frac{1}{\omega_{nl}^2 - \omega^2 + i\gamma\omega}$ and the NF is $\omega_{nl}^2 = \omega_0^2 + \frac{3}{2}\varepsilon\left|\tilde{A}\right|^2$.

Figure 2.3 shows the AR ILM amplitude as a function of the driver frequency F in a driven micromechanical cantilever array with hard nonlinearity. Two bifurcations have been observed at the edges of the stable ILM region as presented in the top trace.

Figure 2.4 shows the linear response spectra for the AR state at different driver frequencies. From bottom to top, the probe spectra are aligned by the driver frequency varying from 140.50 Hz to 144.85 kHz in 50 Hz intervals. The higher frequency (right) sideband is the NF while the lower frequency (left) one is its four-wave mixing

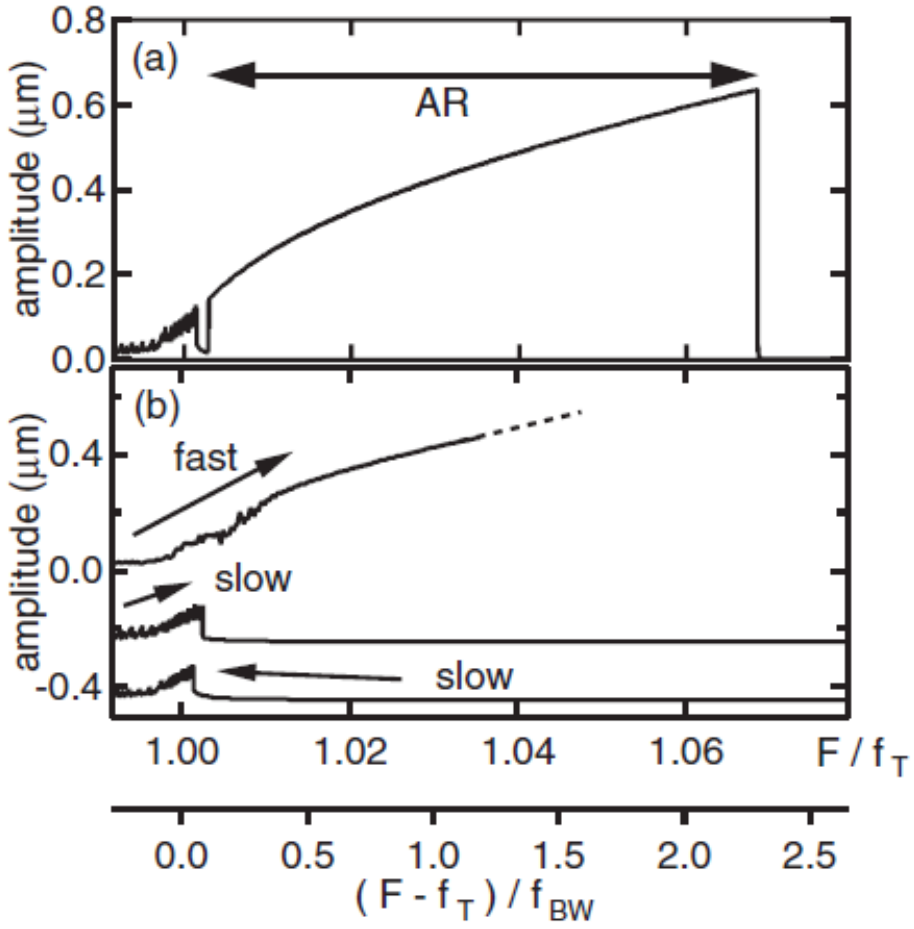

Figure 2.3: Experimentally observed AR amplitude as a function of the driver frequency F. The stable AR ILM region indicated in the top trace is 140.46 to 144.85 kHz.

partner. The NF frequency comes close to the driver frequency as the bifurcations approach. Sato et al. have demonstrated that the NF plays important but different roles in these two bifurcations. The softening of the NF beat frequency leads to the upper bifurcation similar to the saddle-node bifurcation of a single driven Duffing oscillator. While the lower transition is due to the coalescence of the four-wave mixing partner of the NF and topmost extended band mode.

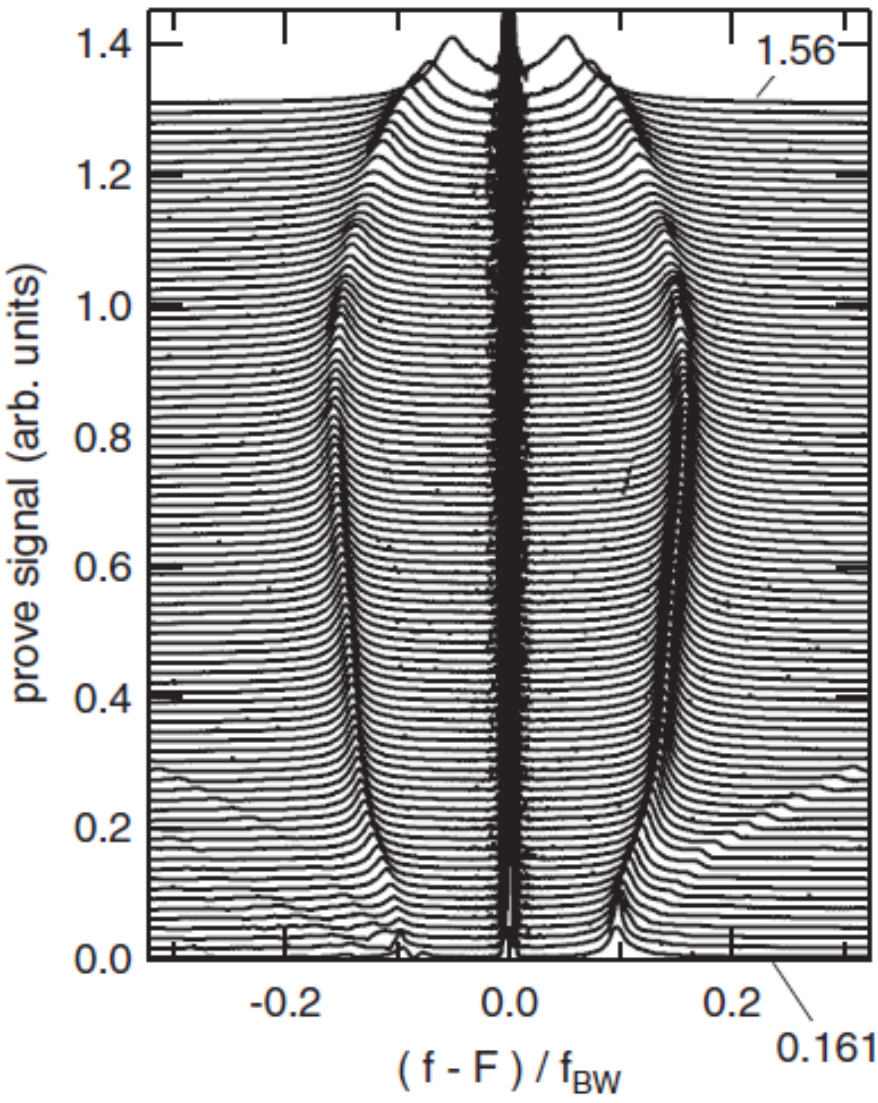

Figure 2.4: Experimental response spectra for the AR state as a function of the normalized different frequency.

References

[1] L. Hadžievski, A. Maluckov, M. Stepic, and D. Kip, *Phys. Rev. Lett.* **93**, 033901 (2004).

[2] M. Sato, S. Imai, N. Fujita, W. Shi, Y. Takao, Y. Sada, B. E. Hubbard, B. Ilic, and A. J. Sievers, *Phys. Rev. E* **87**, 012920 (2013).

Chapter 3

Experimental measurements

3.1 The nonlinear electrical lattice containing MOS-capacitor

In the nonlinear lattice researchers have been investigating ILMs by using a diode as the nonlinear electrical element. The capacitance of the diode, which varies with applied voltage, can be separated into junction capacitance and diffusion capacitance. The junction capacitance dominates for reverse-biased diodes, which has been used for some research on both solitons [1–3] and ILMs [4–6], while diffusion capacitance dominates the forward-biased diode [7] producing a soft nonlinearity for the study of ILMs [8].

Here, instead of diode we employed a MOS-capacitor as the nonlinear element to study ILMs. With the applied DC voltage sweeping slowly from a minus value to a suitable plus voltage, the state of the MOS-capacitor changes as follows: accumulation, depletion, and inversion. From depletion to inversion, the capacitance increases

suddenly and almost immediately achieves a saturation state. [9]

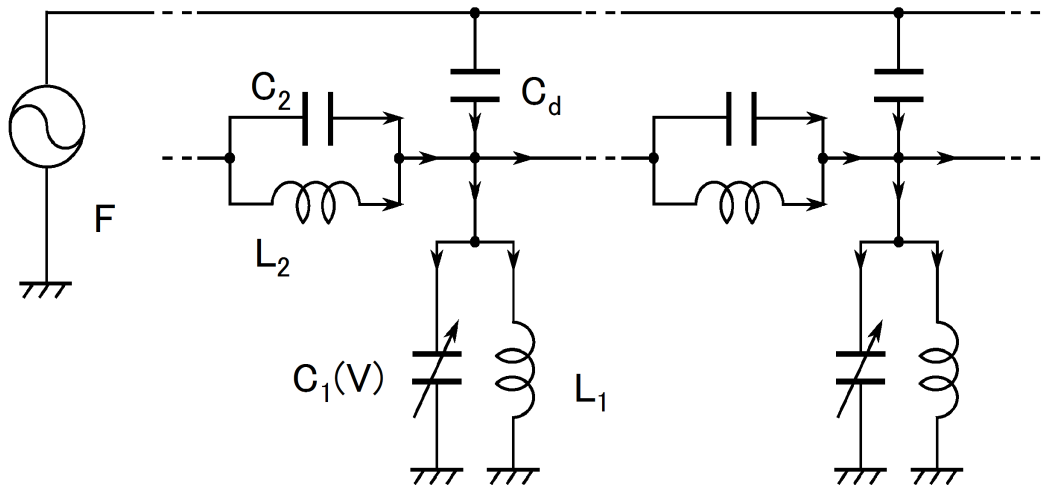

Figure 3.1: Schematic diagram of the nonlinear electrical lattices. One unit cell contains a coupling element, C_2 and L_2, and a nonlinear resonating MOS-capacitor, C_1 and L_1. An AC oscillator with frequency F is used to drive the lattices uniformly through a small-coupling capacitor C_d.

Figure 3.1 shows the experimental design for generation of ILMs in the nonlinear electrical lattice. The nonlinear electrical lattice is made from 16 unit cells, each cell is composed of a nonlinear resonator made by a nonlinear MOS-capacitor C_1, a coil ($L_1 = 313$ μH) and a linear coupling element formed by a capacitor ($C_2 = 421$ pF) and an inductor ($L_2 = 626$ μH). The linear coupler is applied here to achieve a narrow bandwidth of the plane-wave modes to support well-defined ILMs. [10] The lattice is excited uniformly by an oscillator at frequency F through a small capacitor ($C_d = 34.3$ pF).

Figure 3.2 shows capacitance as a function of the applied DC voltage of the MOS-capacitor. To make the capacitance symmetric, the MOS-capacitor is composed of

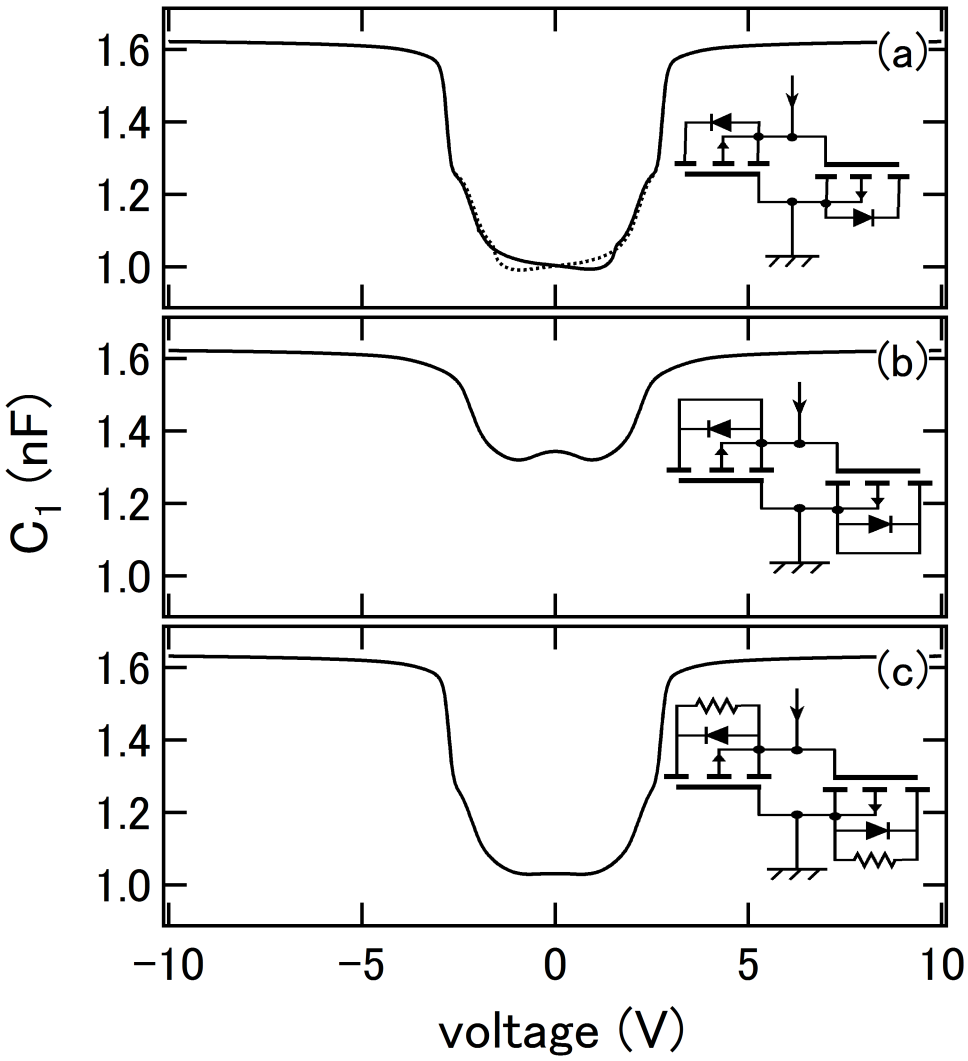

Figure 3.2: DC voltage dependence of the capacitance of C_1. The solid curve is obtained by -10V to 10V scanning and the dotted curve is measured by decreasing the bias voltage from 10V to -10V. Two curves overlap in (b) and (c). As shown in the inset, (a) Two FETs connect parallel and oppositely with drain open. (b) Two anti-paralleled FETs with source-drain connecting. (c) Connecting source and drain with an external resistor.

two anti-paralleled MOS-FETs with drain terminal open as shown in the inset in Fig. 3.2(a). It shows a larger capacitance at both sides of DC bias voltage, because of accumulation or inversion states of a semiconductor below an oxide layer of the MOS. At the middle of the curve, capacitance is small by the depletion state. Since the capacitance increases with absolute voltage, the resonance frequency decreases with increasing amplitude which implies that the MOS-capacitor has soft nonlinearity. The sudden saturation of the MOS capacitance is the key for the variable-width ILMs, since the nonlinearity decreases abruptly when the vibration amplitude is higher than the threshold voltage. To have a larger nonlinear capacitance, we used the high power MOS-FET ($2SJ680$) that has a larger gate capacitance. However, as shown in Fig. 3.2(a) a small hysteresis occurs at the bottom of the curves because of the electric charge in the drain terminal. To discharge the stored charge in the drain electrode, we connected the drain and the source electrode as shown in the inset in Fig. 3.2(b). Although no hysteresis is observed in the curves in Fig. 3.2(b), the capacitance does not change extremely as in the drain open state. Therefore the source-drain connection can not provide enough nonlinearity to generate variable-width ILMs. Then an external resistor ($1.2k\Omega$) is used to connect source and drain electrode for discharging stored charge in the drain terminal as shown in the inset in Fig. 3.2(c). The capacitance curve in Fig. 3.2(c) is almost the same as in Fig. 3.2(a), however, without hysteresis. Thus we applied this connection in our experiments.

Figure 3.3 shows the linear dispersion curve for the electrical lattice. Since the nonlinearity of MOS-capacitor is soft, an ILM can be generated below the bottom of the plane wave band. The dashed line indicates a typical frequency of ILM generation.

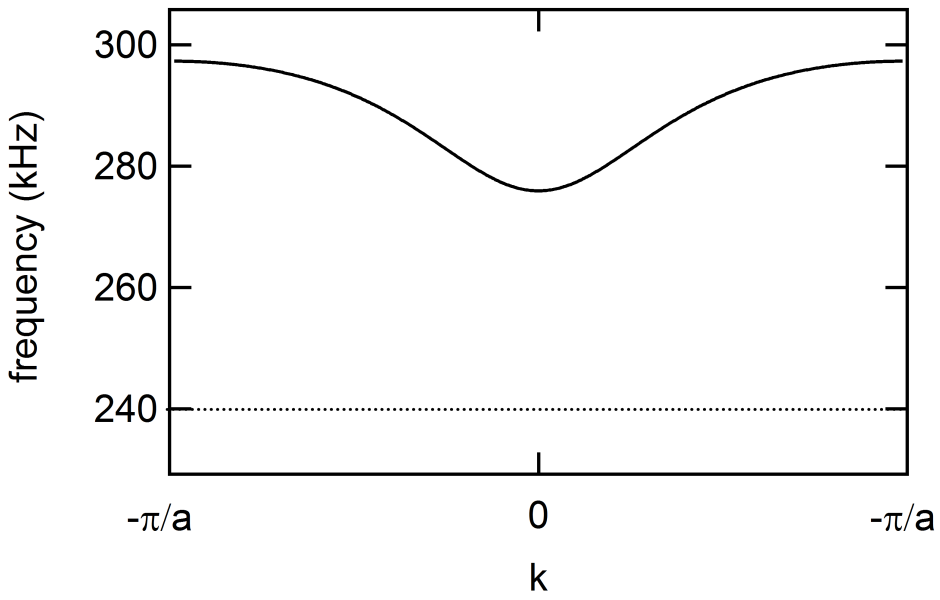

Figure 3.3: Linear dispersion relation curve for this 16 element electrical lattice. Below the bottom of the band, a typical frequency for ILM generation is indicated by dashed line.

3.2 Experimental results: variable width ILM

The experimental procedure is as follows: first, the cw driver excites the nonlinear electrical lattice; then, the voltage of the MOS-FETs at each site is measured by an oscilloscope through a 16 channel analog multiplexer. For clarity only the absolute value of the AC voltage amplitude at each site is monitored. The localized voltage responses as a function of the driver frequency in three patterns with different starting conditions are shown in Fig. 3.4: (a) starting from an initial ILM state at 242 kHz, (b) starting from the ILM at 232 kHz and (c) starting from no ILM state at 229.5 kHz. A darker image indicates a larger oscillating amplitude. The initial ILM was seeded by using an external impurity capacitor (270 pF) at a fixed the driver frequency below the bottom of the linear band frequency (275.9 kHz). After removing the impurity slowly by decreasing the capacitance, the ILM remains at the impurity location. Once an ILM is generated, it is phase locked to the driver; by which to compensate the damping of the nonlinear system. A stable ILM is observed between 230.5 kHz and 244.3 kHz as shown in Fig. 3.4(a) and (b). Below the lower value, the ILM disappears and above the higher value, the ILM vanishes in the standing wave patterns. Without seeding, an ILM also can be generated by scanning up from a low driver frequency. The ILM appears at around 243.5 kHz as shown in Fig. 3.4(c).

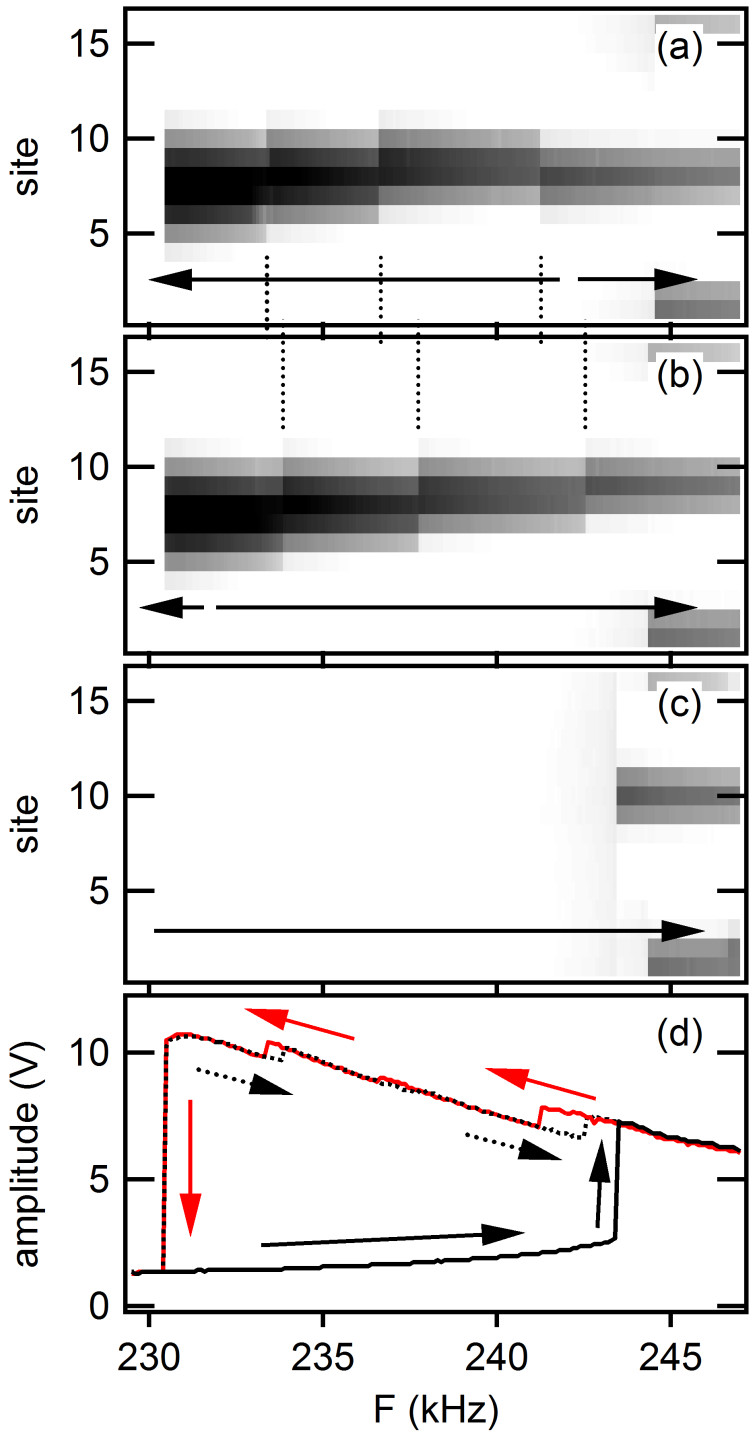
(a)
(b)
(c)
(d)
site
site
site
amplitude (V)
F (kHz)
15
10
5
0
230
235
240
245

Figure 3.4: The voltage amplitude at the different lattice points as a function of the driver frequency. Darker represents a larger voltage. Arrows indicate frequency scanning directions. Vertical dashed lines denote frequencies of transitions. (a) The driver frequency was up-scanned or down-scanned from an ILM state at a high frequency (242 kHz). The initial ILM was seeded by using an impurity capacitor. As decreasing the driver frequency, the width of the ILM changes in a step-widening modality and the shape transforms alternately between bond-centered and site-centered. As the driver frequency is increased, the ILM disappears in the fixed, stationary wave pattern. (b) The frequency was scanned down or up from a low frequency (232 kHz). (c) Increasing the driver frequency from a low frequency below the stable ILM region. The ILM appears around 243.5 kHz and vanishes in standing wave patterns immediately. (d) The maximum amplitude among the lattice points as a function of the driver frequency. The upper red solid trace, the upper dashed trace and the lower trace correspond to Fig. 3.4(a), (b), and (c), respectively.

Step-widening and step-narrowing of the ILM in the stable frequency region are shown in Fig. 3.4(a) and Fig. 3.4(b), respectively. The position of the ILM alternates between band-centered and site-centered locations over the autoresonant range. In these two different processes, step-widening and step-narrowing transitions occur at different frequencies as indicated by the vertical dashed lines. Fig. 3.4(d) shows a summary of the maximum amplitude in Fig. 3.4(a)-(c) as a function of the driver frequency, F. The entire amplitude curve looks very similar to that of a Duffing resonator with negative nonlinearity, except saw-teeth structure in the stable ILM region. Besides of this Duffing like hysteresis, several small hysteresis changes are seen at each step of width varying transition.

An additional weak probe oscillator at frequency f_p is necessary to the linear response measurement. For the purpose of observing all normal modes associated with the ILM, the probe perturbation is only applied at one lattice site contiguous to ILM and the output signal of the other site next to ILM is measured by a lock-in amplifier as shown in Fig. 3.5. The driver frequency is changed slowly inside the stable ILM region and the probe frequency is scanned slowly in an appropriate frequency range at each driver frequency. In order to avoid destroying the ILM state, the amplitude of the probe is set about 1/200 of the driver.

The results of the linear response measurements are displayed in Fig .3.6(a) and (b), for down and up scans, respectively. From bottom to top, the probe spectra are aligned by the driver frequency varying from 244 kHz to 230.6 kHz in 0.2 kHz intervals. Since the ILM occurs below the linear band, the peak on the lower frequency side of the ILM in each trace is the natural frequency (NF) of the ILM. The NF frequency difference decrease as decreasing the driver frequency. The peaks on the

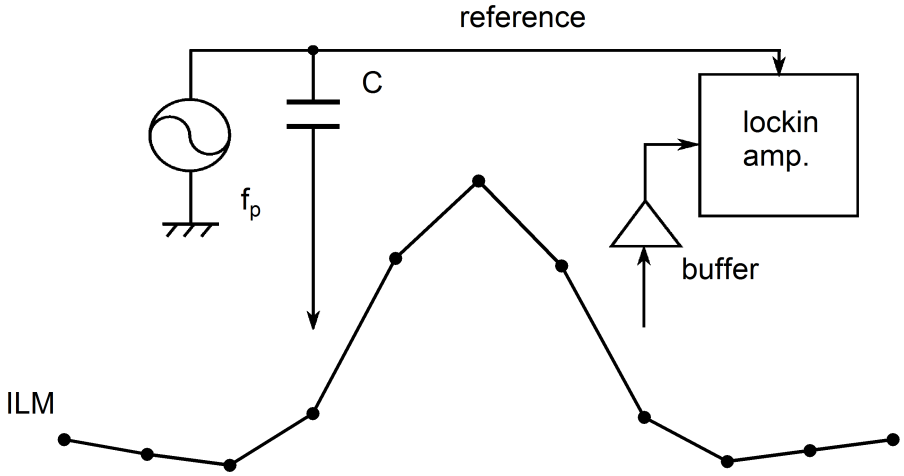

Figure 3.5: Experimental set up for the linear response measurement. Probe perturbation is added to one lattice point next to the ILM through a capacitor and a lock-in amplifier is used to analyze the output signal from the other side of the ILM. The probe amplitude is about 1/200 of the driver and the coupling capacitor is 2 pF.

high frequency side of the ILM are linear local modes (LLMs) and the linear band. To differentiate band and the LLMs, vibration shapes of each mode was investigated. (See the discussion chapter). The peaks marked by 1st, (A), (B), (C), and (D) are the LLMs. We call the LLM closest to the ILM the 1st-LLM. As the driver frequency changes, the peaks of the LLMs move slowly, however, they jump at each step transition. For the down scans, the band mode jumps to a higher frequency at the step transitions while this phenomenon was not observed in case of up scans as indicated by red dotted lines in Fig. 3.6. One novel phenomenon seen in the Fig. 3.6 is an appearance or disappearance of a new LLM at each step transition.

The frequency difference of the linear modes with respect to the driver frequency are summarized in Fig. 3.7. Red and black marks are for the down scanning, Fig.

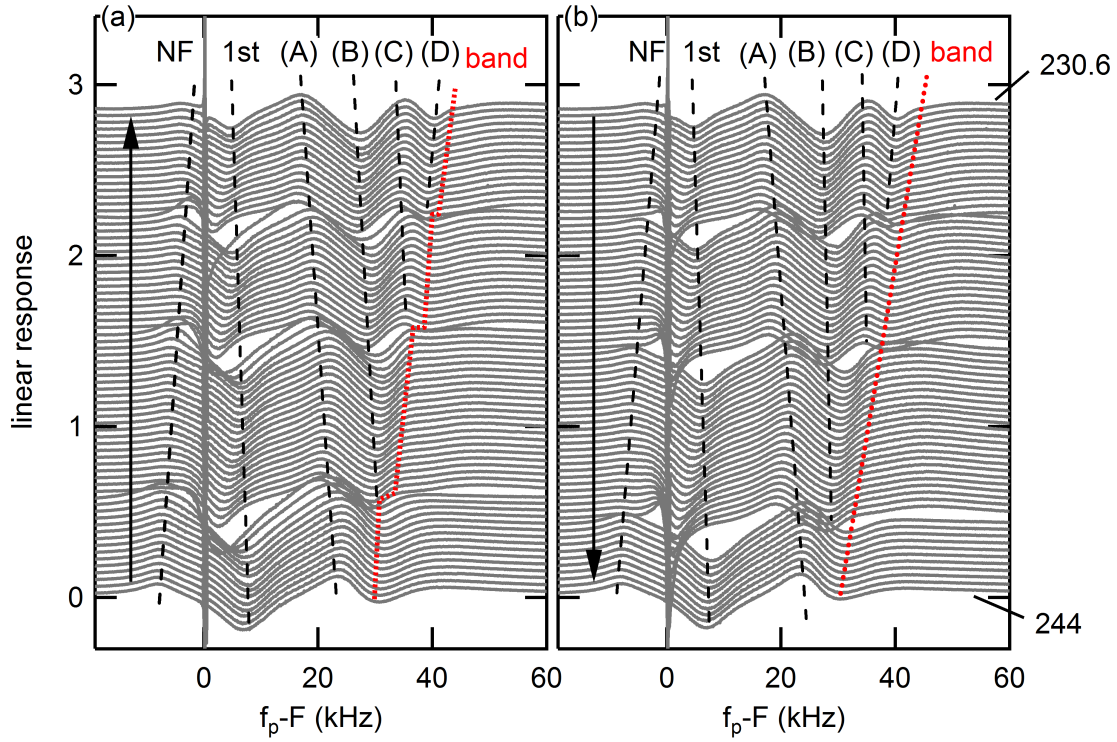

Figure 3.6: Experimental imaginary part of the linear response for the ILM state as a function of the difference frequency between probe f_p and driver F. The driver frequency is down-scanned in (a) from 244 kHz to 230.6 kHz with 0.2 kHz step, and up-scanned in (b) as denoted by arrows. NF is the natural frequency of the ILM and 1st is the linear local mode (LLM) closest to the ILM (We named it 1st-LLM). Peaks indicated by (A), (B), (C), and (D) are other LLMs. The LLMs are located between the ILM and the band mode, and newly generated when the ILM width increased stepwise.

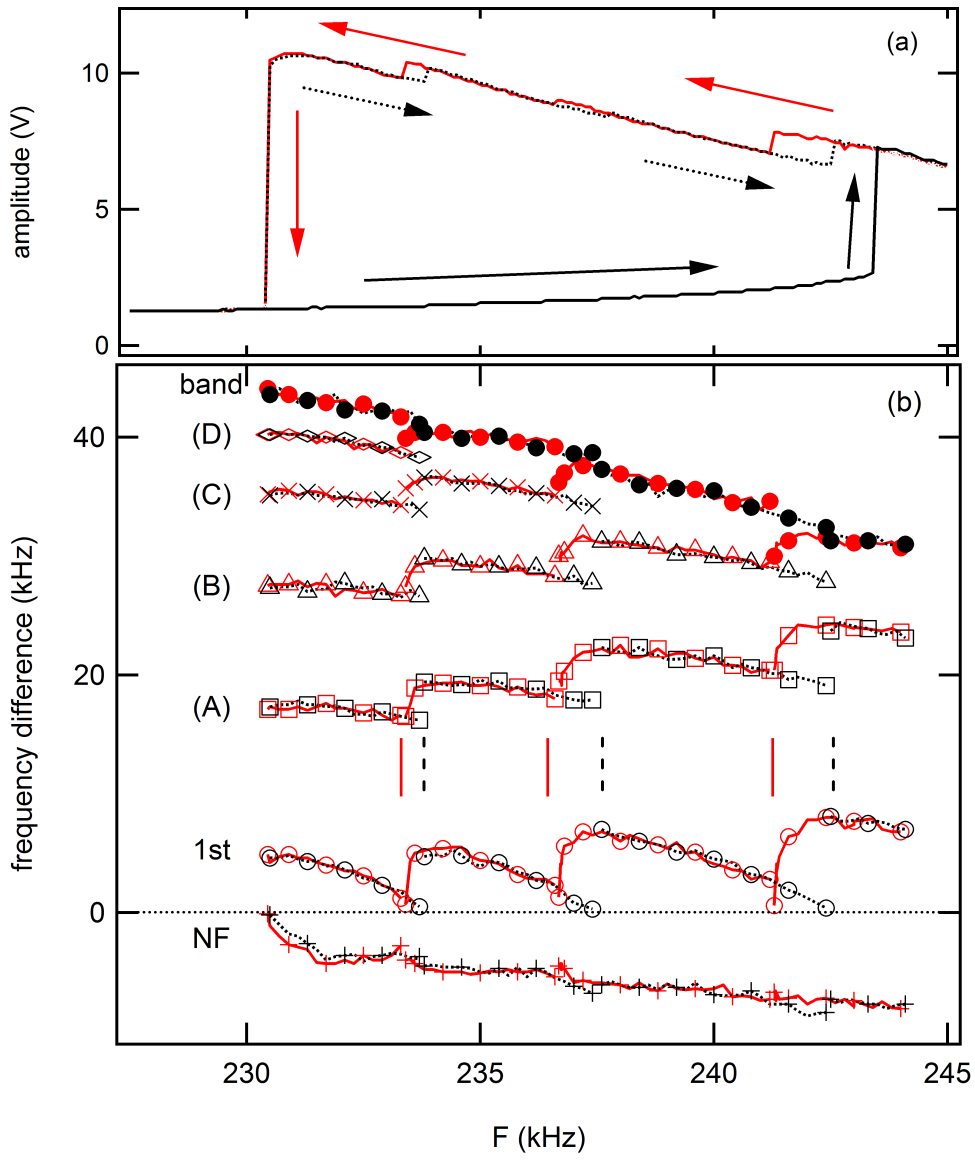

Figure 3.7: (a) The maximum amplitude among the lattice points as a function of the driver frequency. (b) NF of the ILM and the LLMs frequency difference as a function of the driver frequency. Bright (red) marks are for the down scanning, Fig. 3.6(a) and black marks are for the up scanning, Fig.3.6(b). NF, 1st, (A), (B), (C), (D), and band correspond to these in Fig. 3.6. Each symbol denotes one normal mode. Vertical solid (dashed) lines between 1st and (A) indicate frequencies of step transitions for down (up) scanning.

3.6(a) and black marks are for the up scanning, Fig. 3.6(b), respectively. Character NF, 1st, (A), (B), (C), (D), and band are the same as in Fig. 3.6. To distinguish the modes, each mode is indicated by a different kind of symbol. The frequencies of step transition in down (up) scanning are denoted by vertical solid (dashed) lines. As approaching the lower end of the stable region, the NF frequency difference decreases. Similar to that found for the saddle-node bifurcation in the Duffing oscillator [11], the lowest transition point occurs when the NF frequency difference goes close to zero. For all the LLMs, their frequency difference initially increase, then decrease as the step transitions approach. Especially for the 1st-LLM, its frequency goes to zero at the frequency of each step transition. That is, the frequency of the 1st-LLM is almost the same as the frequency of the ILM. Therefore, at such a point the ILM is significantly affected by the 1st-LLM and its width changes since the 1st-LLM corresponds to the lateral vibration of the ILM. Only the band mode closest to the ILM was investigated and marked by band as shown in Fig. 3.6(b). As decreasing the driver frequency, its frequency difference increases slowly, decreases near the step transitions, and then, jumps at the step transitions. In addition, the band mode is very close to the newly generated LLM around the step transitions.

References

[1] T. Kuusela, *Chaos, Solitons Fractals* **5**, 2419 (1995).

[2] B. Z. Essimbi and D. Jager, *J. Phys. D*, **39**, 390 (2006).

[3] J. T. Pan, W. Z. Chen, F. Tao, and W. Xu, *Phys. Rev. E* **83**, 016601 (2011).

[4] R. Stearrett and L. Q. English, *J. Phys. D* **40**, 5394 (2007).

[5] L. Q. English et al., *Phys. Rev. E* **81**, 046605 (2010).

[6] L. Q. English et al., *Phys. Rev. Lett.* **108**, 084101 (2012).

[7] R. Van Buskirk and C. Jeffries, *Phys. Rev. A* **31**, 3323 (1985).

[8] M. Sato et al., *Europhys. Lett.* **80**, 30002 (2007).

[9] K. Dieter and Schroder, *Semiconductor material and device characterization* **2nd** ed, (John Wiley & Sons, New York, 1998), Chap. 6.

[10] K. Fukushima, M. Wadati, and Y. Narahara, *J. Phys. Soc. Jpn.* **49**, 1593 (1980).

[11] M. Sato, S. Imai, N. Fujita, W. Shi, Y. Takao, Y. Sada, B. E. Hubbard, B. Ilic, and A. J. Sievers, *Phys. Rev. E* **87**, 012920 (2013).

Chapter 4

Numerical simulations

4.1 The model of simulation

To compare with experiments we have performed numerical simulation. The numerical model is based on the nonlinear lattice as the same as in experiments. A set of the fundamental equations for the nth cell of the nonlinear electrical lattice shown in Fig. 3.1 is given by [1]

$$\begin{aligned}
&L_2 \frac{\partial i_{L_2,n}(t)}{\partial t} = V_{n-1}(t) - V_n(t), \\
&i_{C_2,n}(t) = C_2 \frac{\partial}{\partial t}[V_{n-1}(t) - V_n(t)], \\
&i_{C_2,n}(t) + i_{L_2,n}(t) = I_n(t), \\
&i_{C,n}(t) = \frac{\partial Q(V_n(t))}{\partial t}, \\
&L_1 \frac{\partial i_{L_1,n}(t)}{\partial t} = V_n(t), \\
&i_{C,n}(t) + i_{L_1,n}(t) = I_n(t) - I_{n+1}(t) + C_d \frac{\partial}{\partial t}(V_d - V_n(t))
\end{aligned} \tag{4.1}$$

Here V_d indicates AC voltage source, $V_n(t)$ the voltage across $C_1(V)$, $i_{L_2,n}(t)$ the current through L_2, $i_{C_2,n}(t)$ the current through C_2, $i_{C,n}(t)$ the current through the

$C_1(V)$, $i_{L_1,n}(t)$ the current through L_1, and $Q(V_n(t))$ the charge in $C_1(V)$. Combining Eqs. 4.1, we obtain

$$\begin{aligned}\frac{\partial^2 Q(V_n(t))}{\partial t^2} &= C_2\frac{\partial^2}{\partial t^2}[V_{n-1}(t) - 2V_n(t) + V_{n+1}(t)] - C_d\frac{\partial^2}{\partial t^2}V_n(t) \\ &+\frac{1}{L_2}[V_{n-1}(t) - 2V_n(t) + V_{n+1}(t)] \\ &-\frac{1}{L_1}V_n(t) + C_d\frac{\partial^2}{\partial t^2}V_d(t).\end{aligned} \tag{4.2}$$

Introducing the damping part of the nonlinear system, Eq. 4.2 becomes

$$\begin{aligned}\frac{\partial^2 Q(V_n(t))}{\partial t^2} &= C_2\frac{\partial^2}{\partial t^2}[V_{n-1}(t) - 2V_n(t) + V_{n+1}(t)] - C_d\frac{\partial^2}{\partial t^2}V_n(t) \\ &+\frac{1}{L_2}[V_{n-1}(t) - 2V_n(t) + V_{n+1}(t)] \\ &-\frac{1}{L_1}V_n(t) - \frac{k_0+k_1}{\tau}\frac{dV_n(t)}{dt} + C_d\frac{\partial^2}{\partial t^2}V_d(t).\end{aligned} \tag{4.3}$$

where $\tau = 41.7$ μs is the damping time estimated by experiments. The capacitance of the nonlinear MOS-capacitor C_1 can be approximated by the form

$$C_1(V) = k_0 + k_1 \exp\left[-(V/k_2)^4\right] \tag{4.4}$$

Where $k_0 = 1.63$ nF, $k_1 = -0.603$ nF, and $k_2 = 2.76$ V. The calculated results from Eq. 4.4 are shown by the dashed curve in Fig. 4.1. Considering the relationship $dQ = C_1 dV$, the left side of Eq. 4.3 becomes

$$\frac{d^2 Q(V_n(t))}{dt^2} = C_1(V_n(t))\frac{d^2 V_n(t)}{dt^2} + \frac{dC_{1(n}(t))}{dV_n(t)}\left(\frac{dV_n(t)}{dt}\right)^2 \tag{4.5}$$

From Eq. 4.4, we obtain

$$\frac{dC_1(V_n(t))}{dV_n(t)} = \frac{-4k_1}{k_2}\left(\frac{V_n(t)}{k_2}\right)^3 \exp\left[-(V_n(t)/k_2)^4\right] \tag{4.6}$$

Substituting Eq. 4.4 and 4.6 into Eq. 4.5

$$\begin{aligned}\frac{d^2 Q(V_n(t))}{dt^2} &= [k_0 + k_1 \exp(-(V_n(t)/k_2)^4)]\frac{d^2}{dt^2}V_n(t) \\ &-\left\{\frac{4k_1}{k_2}\left(\frac{V_n(t)}{k_2}\right)^3 \exp\left[-(V_n(t)/k_2)^4\right]\right\}\left(\frac{dV_n(t)}{dt}\right)^2\end{aligned} \tag{4.7}$$

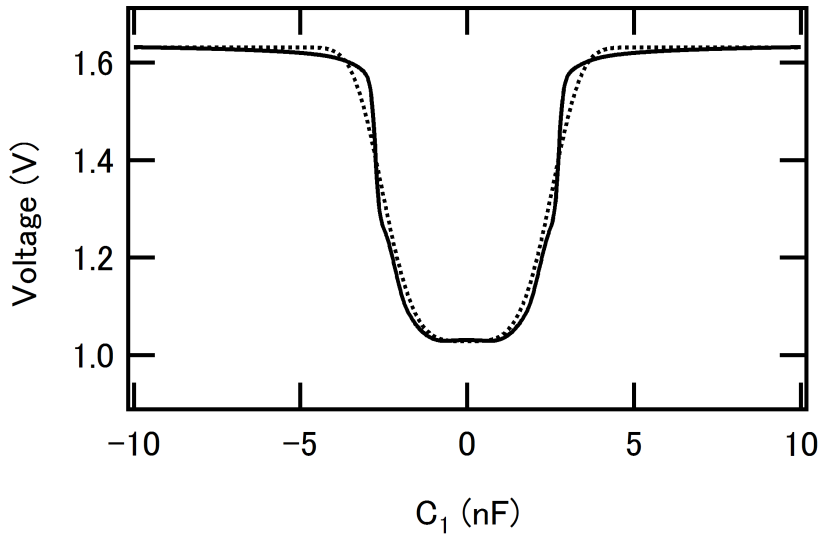

Figure 4.1: DC voltage dependence of experimental and simulated $C_1(V)$. The solid curve is the same as shown in Fig. 3.2(c) that measured from experiments and the dashed curve is $C_1(V)$ model calculated by Eq. 4.4).

To summarize Eq. 4.3 and 4.7, finally the model of the nonlinear electrical lattices used for simulations is built on the form [2]

$$\begin{aligned}[k_0 + k_1 \exp(-(V_n(t)/k_2)^4)]\, \tfrac{d^2}{dt^2} V_n(t) - \left\{ \tfrac{4k_1}{k_2} \left(\tfrac{V_n(t)}{k_2}\right)^3 \exp\left[-(V_n(t)/k_2)^4\right] \right\} \left(\tfrac{dV_n(t)}{dt}\right)^2 \\ = C_2 \tfrac{\partial^2}{\partial t^2}[V_{n-1}(t) - 2V_n(t) + V_{n+1}(t)] - C_d \tfrac{\partial^2}{\partial t^2} V_n(t) \\ + \tfrac{1}{L_2}[V_{n-1}(t) - 2V_n(t) + V_{n+1}(t)] \\ - \tfrac{1}{L_1} V_n(t) - \tfrac{k_0+k_1}{\tau} \tfrac{dV_n(t)}{dt} + C_d \tfrac{\partial^2}{\partial t^2} V_d(t).\end{aligned} \tag{4.8}$$

Here, the values of k_0, k_1, and k_2 are given above and other parameters are exactly the same as in experiments mentioned in Chap. 3.

If we only consider the linear part, Eq. 4.8 becomes

$$\begin{aligned}[k_0 + k_1] \tfrac{\partial^2 V_n(t)}{\partial t^2} = C_2 \tfrac{\partial^2}{\partial t^2}[V_{n-1}(t) - 2V_n(t) + V_{n+1}(t)] - C_d \tfrac{\partial^2}{\partial t^2} V_n(t) \\ + \tfrac{1}{L_2}[V_{n-1}(t) - 2V_n(t) + V_{n+1}(t)] - \tfrac{1}{L_1} V_n(t)\end{aligned} \tag{4.9}$$

Then the linear dispersion relation for the nonlinear electrical lattice has the form

$$\omega^2 = \frac{\frac{2}{L_2}(1-\cos ka) + \frac{1}{L_1}}{2C_2(1-\cos ka) + C_d + k_0 + k_1} \tag{4.10}$$

The results of the calculation of Eq. 4.10 are shown in Fig. 3.3.

4.2 Simulated results

Calculation results of Eq. 4.8 plotted by the driver frequency dependent amplitude are shown in Figures 4.1(a)-(c). Compared with the experiments, these patterns are measured from different starting conditions: (a) starting from an initial ILM state at 245.5 kHz, (b) starting from the ILM at 233.5 kHz and (c) starting from no ILM state at 232 kHz. As the same in the experiments, the initial ILM was generated by introducing and removing impurity capacitor. In Fig. 4.1(a), the stable ILM region is from 233 kHz to 246 kHz. Outside this region ILM is replaced by standing waves or disappears. Inside the stable region, similar to the experiments, the ILMs widens stepwise as the driver frequency decreases. Fig. 4.1(b) shows the scanning in an opposite direction. However, different from the experiments, ILM cannot be generated by scanning up from a low frequency. Instead, the standing waves appear at 245 kHz, inside the stable ILM region. Fig. 4.1(d) shows a summary of the maximum amplitude in Figures. 4.1(a)-(c) as a function of the driver frequency, F. Several tiny hysteresis loops between step widening and narrowing transitions are observed while they are much smaller than in the experiments. In other words, the difference between down and up scans in the simulations can be ignored. Therefore, only the linear response spectra of down scans were investigated below.

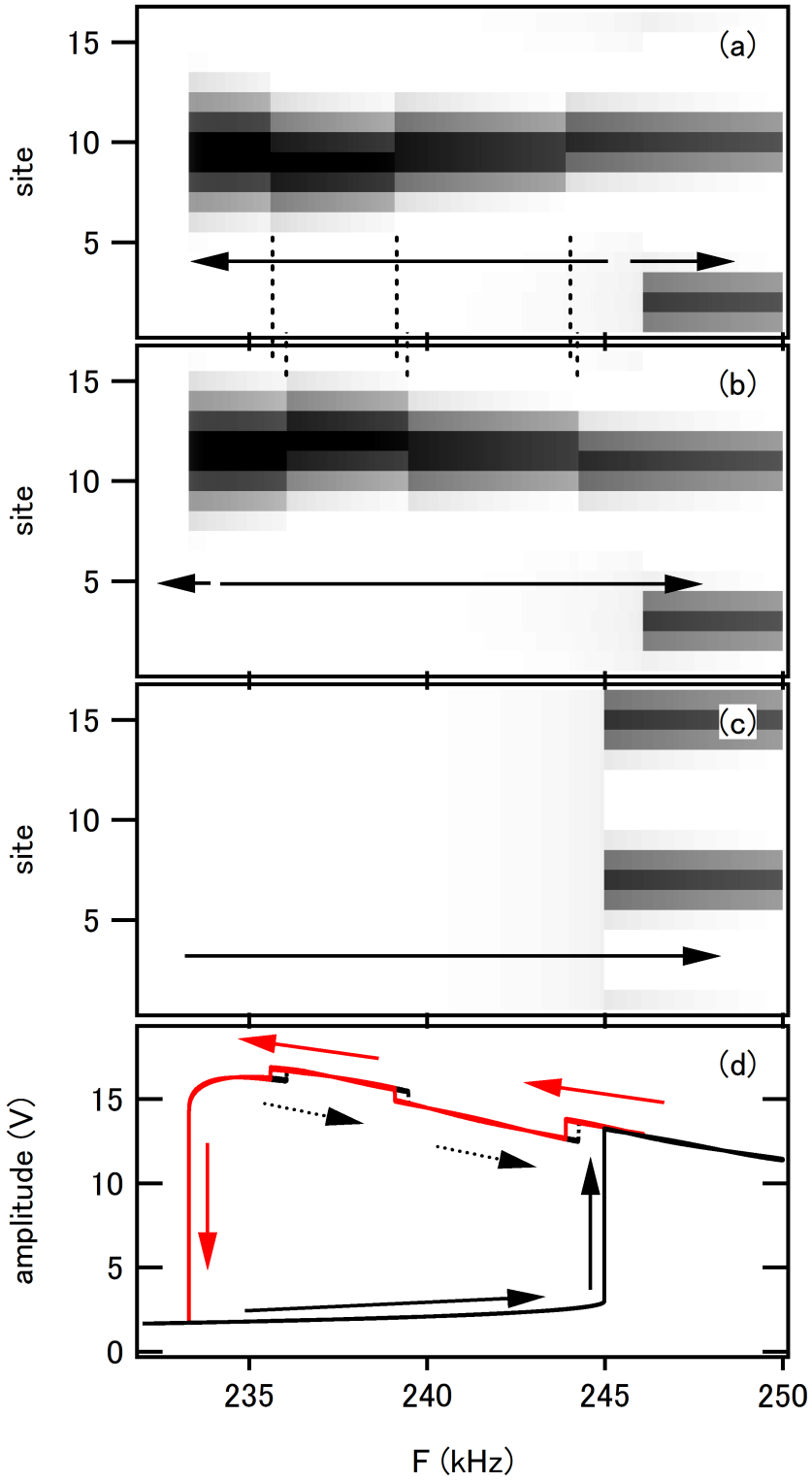
(a)
(b)
(c)
(d)
site
site
site
amplitude (V)
F (kHz)
15
10
5
0
235
240
245
250

Figure 4.1: Simulation results calculated by Eq. 4.8. (a) The voltage amplitude as a function of the driver frequency. Darker represents a larger voltage. Similar to the experiments, the driver frequency was scanned up or down from an ILM state at a high frequency (245.5 kHz). As indicated by arrows. Vertical dashed lines denote frequencies of transitions. (b) The frequency was scanned down or up from a low frequency (233.5 kHz). (c) Increasing the driver frequency from a low frequency below the stable ILM region. (d) The maximum amplitude among the lattice points as a function of the driver frequency. The upper red solid trace, the upper dashed trace and the lower trace correspond to Fig. 4.1(a), (b), and (c), respectively.

The method of the calculation of the linear response spectrum is similar to the experiments. First, the ILM is generated. Then, a weak probe oscillator (10^{-5} of the driver) is applied to the site next to the ILM. Voltage at the other site adjacent to the ILM is multiplied by cosine and sine functions vibrating with the probe frequency fp and averaged over a certain time. To eliminate the large ILM component, two set of simulations with opposite phases of the probe driver are made, and difference between them is calculated. The details of the linear response calculation are given in Ref. [3].

The imaginary part of the linear response spectra in the case of down scans are presented in Fig. 4.2. Here, we only focus on the movement of frequency difference as the driver frequency changes. The traces are for different driver frequencies, from bottom to top, varying from 246 kHz to 233.4 kHz in 0.2 kHz intervals. By investigating the vibration shapes (see the discussion chapter), it is known that the peak marked by NF is the natural frequency of the ILM, 1st is the 1st-ILM associated the ILM, (A)-(D) are other LLMs, band is one of the band modes closest to the ILM, and the peaks on the right hand of band are other band modes. As the driver frequency decreases, the NF comes close to the ILM and the LLMs have a tendency of softening. For the band mode, it jumps away from the ILM at each step transition. Moreover, a new LLM would be generated as the ILM occupies one more site. Those findings coincide with the experimental results in the case of down-scanning.

The frequency differences of the linear modes with respect to the driver frequency are shown in Fig. 4.3(b). As in the experiment, the modes are differentiated by symbols. The NF of the ILM softens as approaching the fundamental bifurcation at the lower end of the stable ILM region. Between two step transitions, the LLMs first

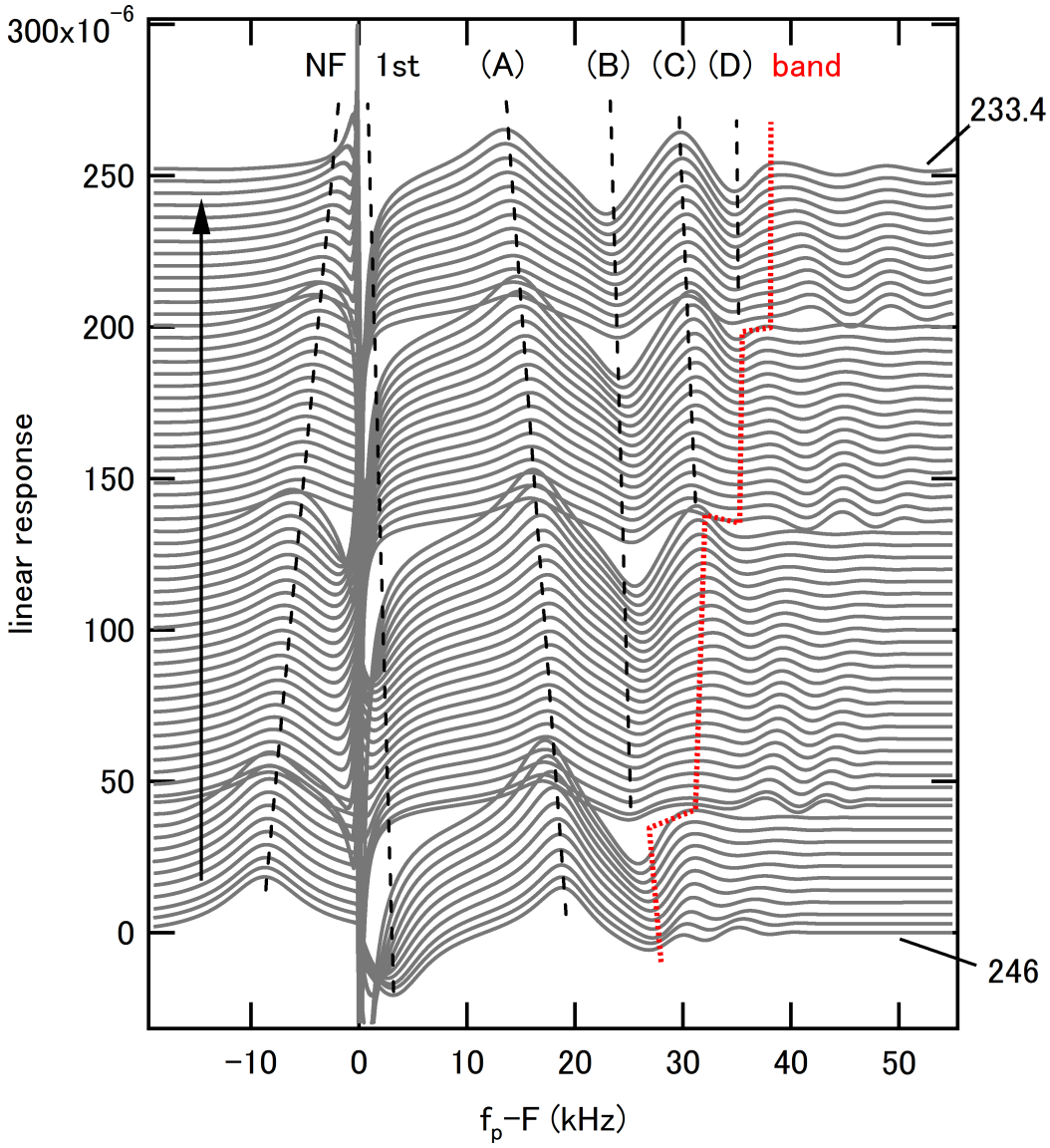

Figure 4.2: Simulated imaginary part of the linear response for the ILM state in the down scans as a function of the difference frequency between the probe f_p and the driver F. From bottom to top, the driver frequency is from 246 kHz to 233.4 kHz with 0.2 kHz/step. The vertical arrow indicates the scanning direction of the driver frequency. Exactly the same as in experiments, NF is the natural frequency of the ILM and 1st is the 1st-LLM. Peaks indicated by (A), (B), (C), and (D) are other LLMs.

increases, then decreases. Because the 1st-LLM is too close to the ILM, it is hard to examine its behavior. Therefore, the scale of the ordinate was adjusted as shown in Fig. 4.3(c). The 1st-LLM difference frequency softens at both sides of a transition. Moreover, its maximum value between every adjacent step transitions decreases extremely as decreasing the driver frequency. For the band mode, its frequency difference makes a leap to a higher frequency. In general terms, the movements of linear modes in simulations are in accordance with the results of the experiments presented in Fig. 3.7(b).

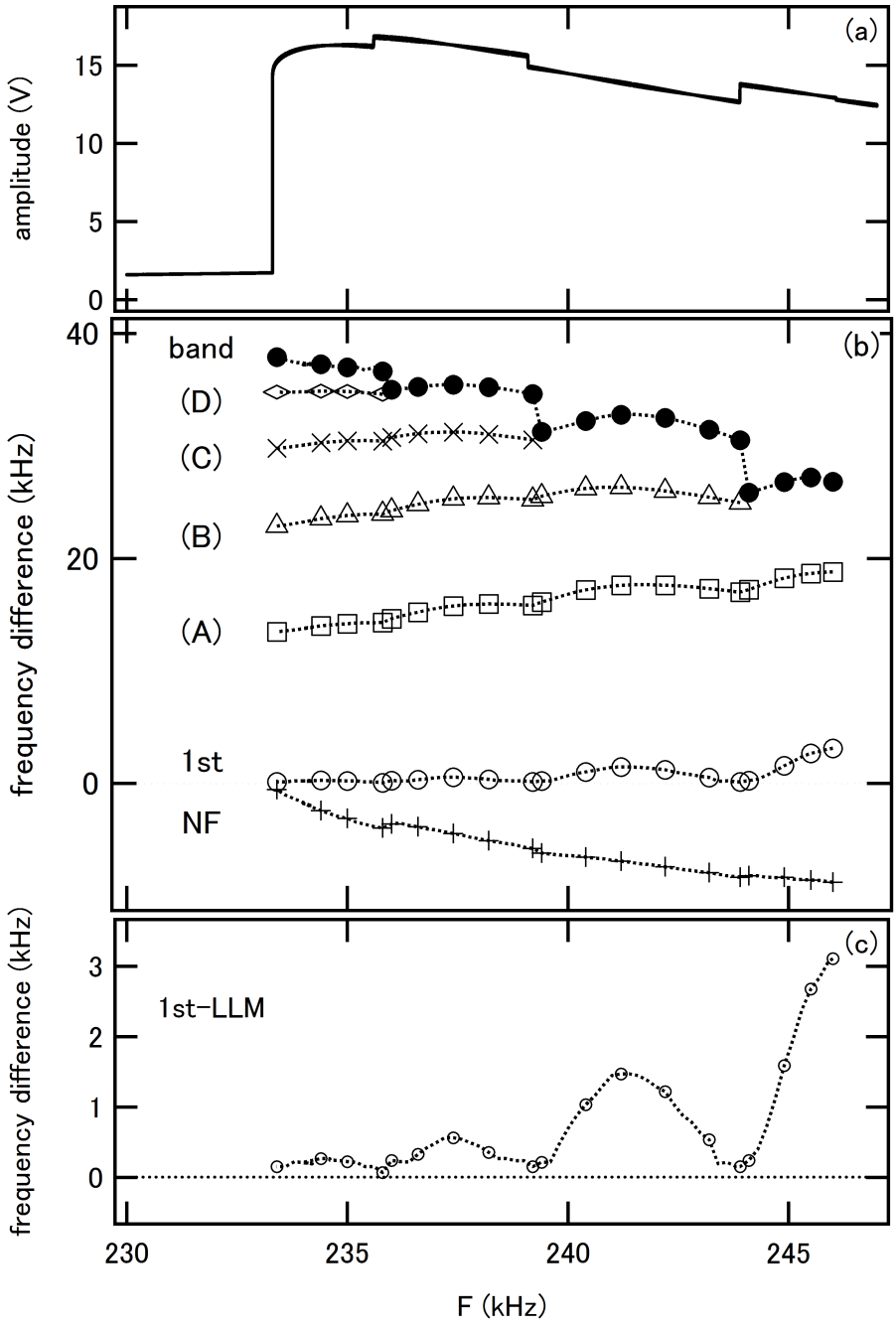

Figure 4.3: (a) Summary of simulation results. (a) The maximum amplitude of the ILM as a function of the driver frequency for the down-scanning. (b) Frequency difference measured from linear responses as a function of the driver frequency. NF, 1st, (A), (B), (C), (D), and band correspond to these in Fig. 4.2. Each symbol denotes one normal mode. (c) 1st-LLM frequency. The movement of 1st-LLM enlarged here for clarity.

References

[1] K. Fukushima, M. Wadati, and Y. Narahara, *J. Phys. Soc. Jpn.* **49**, 1593 (1980).

[2] W. Shi, S. Shige, Y. Soga, M. Sato, and A. J. Sievers, *Europhys. Lett.* **103**, 30006 (2013).

[3] M. Sato, S. Imai, N. Fujita, W. Shi, Y. Takao, Y. Sada, B. E. Hubbard, B. Ilic, and A. J. Sievers, *Phys. Rev. E* **87**, 012920 (2013).

Chapter 5

Discussions

5.1 Stepwise varying width of the ILM.

The observations of step-widening (-narrowing) ILM have been achieved in the nonlinear electric lattice by using MOS-capacitors with saturable nonlinearity. In the theoretical work, Hadžievski and coworkers have demonstrated that in the DNLS lattices with saturable nonlinearity site-centered and bond-centered ILM alternates as power increases as shown in Fig. 2, Ref. [1]. In order to facilitate figurative understanding of the behavior of the ILM, amplitude plot is presented in Fig. 5.1 by measuring the amplitudes at power 10, 50, 100, and 160 in Fig. 2 of Ref. [1]. Hence, it is clear that our experimental findings shown in Fig. 3.2(a) are in accordance with the theoretical work [1]: the ILM expands as its amplitude increases.

In addition, they have also explained that the interchange of stability between site-centered and bond-centered states is attributed to the PN barrier height in Fig. 1, Ref. [1]. When the PN barrier is zero the ILM location exchanges between site-

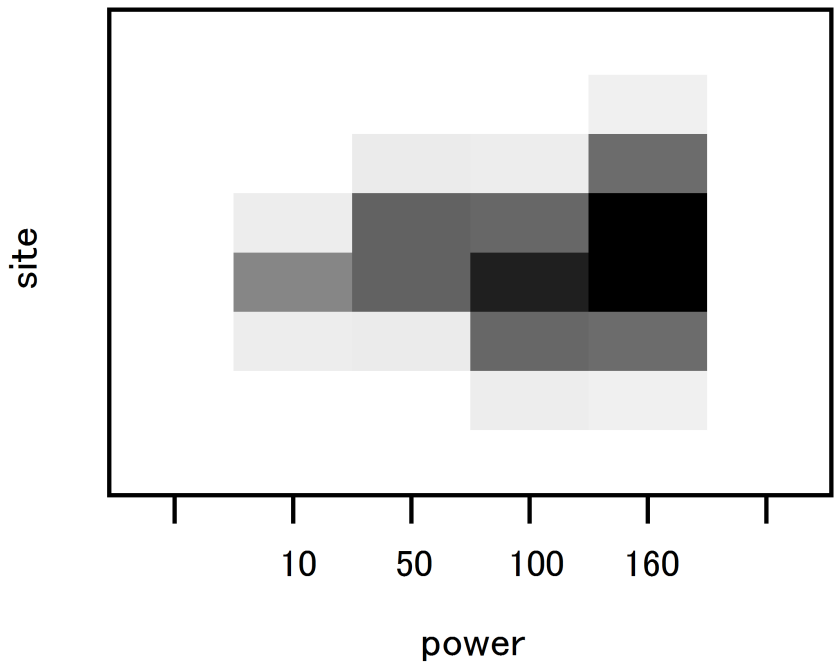

Figure 5.1: Amplitude plot as a function of power adapted from Fig. 2 of Ref. [1]. Darker is larger amplitude.

centered and bond-centered. That is, the ILM can move freely at the transition points with zero PN potential. In our experiments, the alternation between site-centered and bond-centered ILM is due to the 1st-LLM since the NF and other LLMs are far away from the ILM as shown in Fig. 3.7(b). The 1st-LLM is related to lateral motion of the ILM. When the 1st-LLM is excited and mixed with the ILM, the ILM oscillates laterally at the frequency difference of them. The ILM is pinned at a lattice site and frequency of the motion around the pinning site is this frequency difference. Thus, the frequency difference of the 1st-LLM measures an effective pinning potential of the ILM. It is known that the pinning potential is relevant to the PN barrier height. Therefore, the softening of the 1st-LLM frequency difference as step transitions approaches corresponds to the decreasing of the PN

barrier height.

The vibration shapes of NF and LLMs are investigated and the results are shown in Fig. 5.2 by the experiments and Fig. 5.3 by the simulations. Both in the experiments and the simulations, these panels are measured at different driver frequencies, each of which is a suitable frequency located between two neighboring step transitions. From left to right, the width of the ILM expands stepwise. The character marks are consistent with these in Fig. 3.7. The vibration shapes are obtained by the similar way to the linear response measurement in experiments besides the probe frequency was set at each peak of the spectra. Then voltage at each site was measured by a lock-in amplifier. The method of vibration shape measurement in the simulations is almost the same as in the experiments except that a subtraction of two simulations with opposite probe phase is necessary to eliminate the large vibration of the ILM.

As shown in Fig. 5.2 and Fig. 5.3, the NF shape is very similar to that of the ILM and 1st-LLM is an even LLM. As the width of the ILM expands, the shape of the NF and the LLMs extends as expected since they are strongly affected by the ILM. [2,3] Here, we only focus on the 1st-LLM because other linear modes have nothing to do the stepwise varying width of the ILM. When the frequency difference between the ILM and the 1st-LLM is large, the 1st-LLM is weak that the lateral oscillation of the ILM is puny. However, as approaching the step transitions, the 1st-LLM becomes very strong because of the resonance with the ILM as shown in Fig. 3.6. In other words, the ILM has a very intense lateral oscillation at the step transitions. Fig. 5.4 shows the enlarged shapes of the ILM and 1st-LLM in the left two panels of Fig. 5.2. In Fig. 5.4(a) the ILM occupies site 8, 9, 10, at which amplitude of the 1st-LLM is plus, near zero, and minus, respectively. At the step transition points, the amplitude

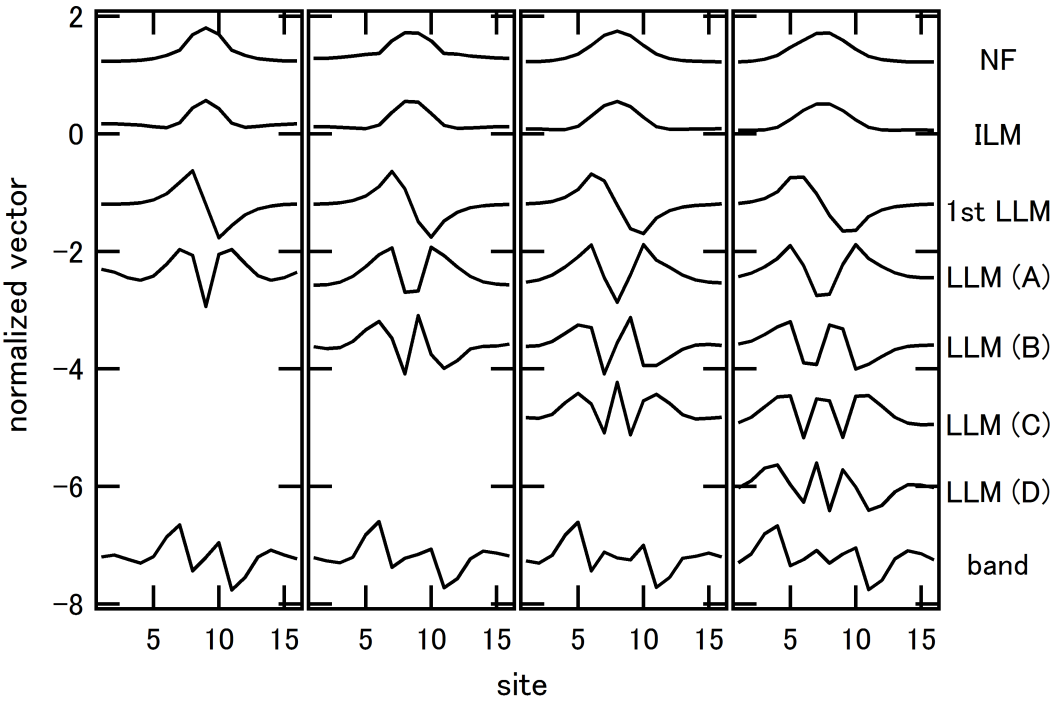

Figure 5.2: Experimental normalized vectors of vibration shapes for each mode at their peak frequencies. From left to right, panels are measured at $F = 243.1$ kHz, 239.4 kHz, 235.2 kHz, and 232.1 kHz, respectively. These frequencies are typical frequency in every region between two neighboring step transitions. Characters are defined the same as in Fig. 3.6 and Fig. 3.6 in Chap. 3.

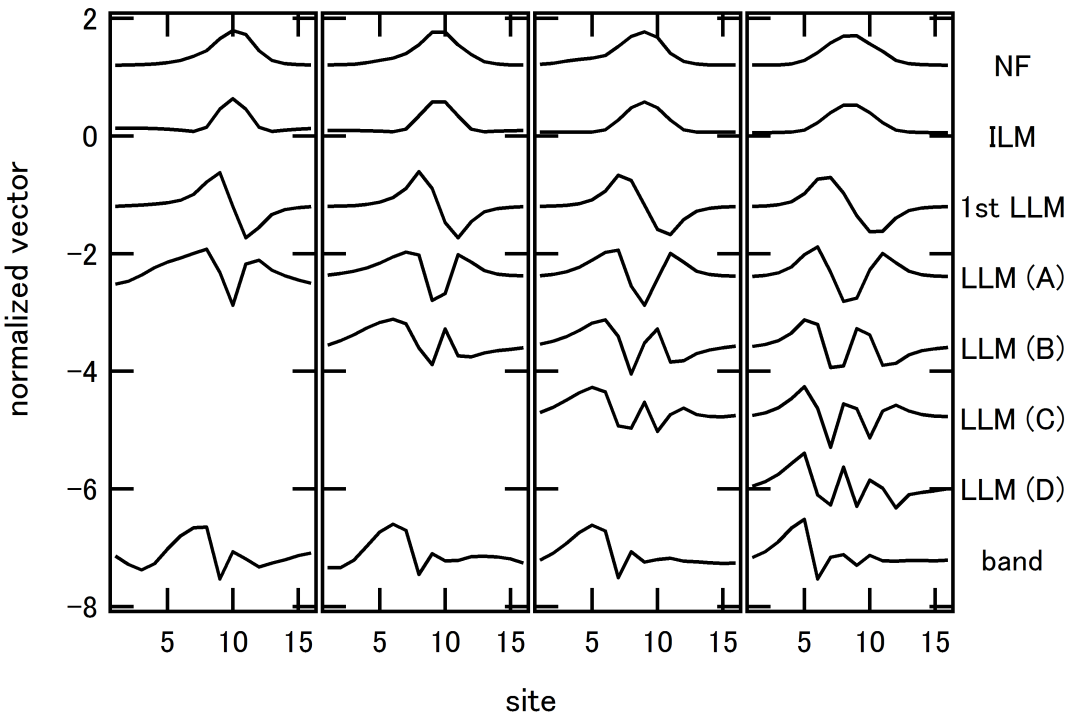

Figure 5.3: Simulated normalized vectors of vibration shapes. Similar to the experiments, each panel is measured at an ILM state with a regular width. From left to right, the driver frequency is 245.5 kHz, 241.8 kHz, 237.6 kHz, and 234.6 kHz, respectively.

of the ILM at site 8 increases while decreases at site10. As a result, the ILM possesses site 7, 8, 9, and 10 after width expansion as shown in Fig. 5.4(b). Such processes give rise to changing the width of the ILM stepwise as shown in Fig. 3.4. It is very clear that the 1st-LLM is the key for the variable width ILM. Simulations show a good agreement with the experimental results.

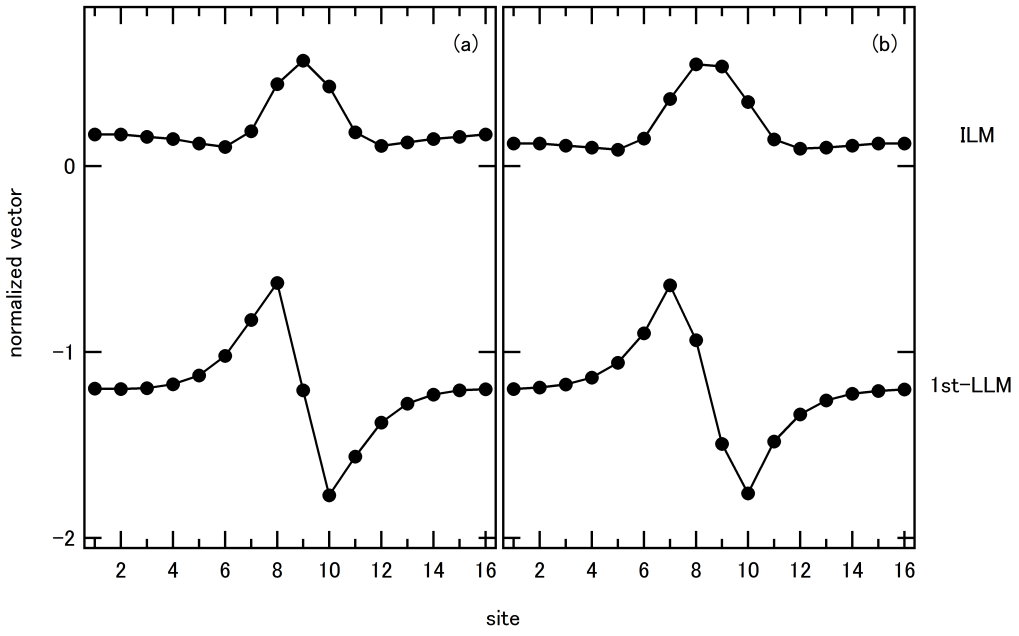

Figure 5.4: Enlargements of the ILM and 1st-LLM shapes in the left two panels in Fig. 5.2.

5.2 The NF and other LLMs

The lower fundamental transition observed at the lower edge of the stable ILM region is similar to the saddle-node bifurcation in the Duffing resonator, which is studied in Ref. [2]. The movements of the NF associated with the ILM in Figs. 3.7(b)

and Fig. 4.3(b) are consistent with the previous study, that is, that saddle node bifurcation accompanies the softening of the NF. The NF also plays an important role in bifurcations of an ILM in a cantilever array, where it measures an effective potential of phase locking to the driver. Thus, the softening of the NF makes the ILM unstable because of unlocking the vibration phase from the driver. [2]

In addition, the shape of the NF is almost the same to ILM in both experiments and simulations, as shown in Fig. 5.2 and Fig. 5.3. It is expected because NF is a vibration in a van der Pol plane around a fixed point for the ILM state. There are only two degrees of freedom, amplitude and relative phase to the driver. Thus, there should be no shape difference. [2]

As shown in Fig. 3.7(b), the frequencies of the LLMs changes with the ILM frequency (amplitude). Compared with the theoretical work in Ref. [3], where by Hizhnyakov et al. have demonstrated that LLMs are induced by the ILM and the movements of their frequencies depend on the ILM amplitude. Moreover, new LLMs are generated as the width of the ILM expands. When the ILM occupies one more site it has an additional degree of freedom. Hence, the linear modes associated with the ILM increases. The additional linear mode is exactly the newly generated LLM. On the other hand, with the expansion of the ILM the degree of freedom of the band decreases, that is, the number of the band modes reduces. It implies that a band mode changes into a LLM at the step transitions since their frequencies are almost the same as shown in Fig. 3.7(b).

Furthermore, the LLMs extend with the widening of the ILM as displayed in Fig. 5.2 and Fig. 5.3, showing that they are greatly influenced by the ILM. The 1st-LLM, LLM (B), and LLM (D) are even mode, and LLM (A) and LLM (C) are odd mode. [3]

Actually, in the stable ILM state, all linear modes can be classified into odd and even symmetries in the terms of the vibrating shape and appear alternatively when ordered by their mode frequency. It can be described as follows: when the ILM occupies only one site, no LLM exists because the ILM keeps this degree of freedom for itself; then, the width of the ILM expands to two sites, the 1st-LLM appears and it must be even mode since the 1st-LLM is the lateral vibration of the ILM in only two sites. Finally, as a consequence, the LLMs alternate between odd and even mode as shown in Fig. 5.2 and Fig. 5.3.

5.3 The hysteresis inside the stable ILM region

The phenomena of hysteresis have been observed both in the experiments and the simulations, as shown in Fig. 3.4 and Fig. 4.1, respectively. The existence of hysteresis indicates the possibility of different mechanisms for down and up scans. It suggests that traveling ILMs cannot be generated in our nonlinear electrical lattice since even at a transition a barriers remains. However, hysteresis in the simulations is much smaller than in the experiments. To get more quantitative information, the maximum amplitudes are summarized in Fig. 5.5 (a) and (b), corresponding to Fig. 3.4(d) and Fig. 4.1(d), respectively. In the direction of the decrement of the driver frequency, frequency regions of hysteresis are 1.3 kHz, 1.1 kHz, and 0.5 kHz in the experiments, while 0.37 kHz, 0.4 kHz, and 0.45 kHz in the simulations. The difference between experiments and simulations is the properties of the nonlinear element, MOS-capacitor. Although we tried our best to fit the C-V curve, there are still some differences between the measured C-V curve and the approximate one as shown in Fig.

4.1. Moreover, as mentioned in Chap. 3, an external resistor is used to connect source and drain electrode for discharging stored charge in the drain terminal. But because of large resistance (1.2 kΩ) of the external resistor the speed of discharging may not be fast enough. A larger hysteresis therefore has been found in the experiments.

For more evidence, hysteresis has been investigated in the case of drain open as shown in Fig. 3.2(a). Fig. 5.6 shows the driver frequency dependent amplitude in three patterns, similar to these in Chap. 3. Here, we focus on the hysteresis. As the driver frequency deceases, hysteresis covers the frequency range: 4.9 kHz, 4.7 kHz, and 4.6 kHz, respectively. Comparing with Fig. 5.5(a), the hysteresis is much larger. Because without external resistor the speed of discharging becomes very slow. While in the simulation, the conditions are ideal so that it is no need to consider the stored charge in the drain electrode. Hence, hysteresis in the simulations is smaller than in the experiments.

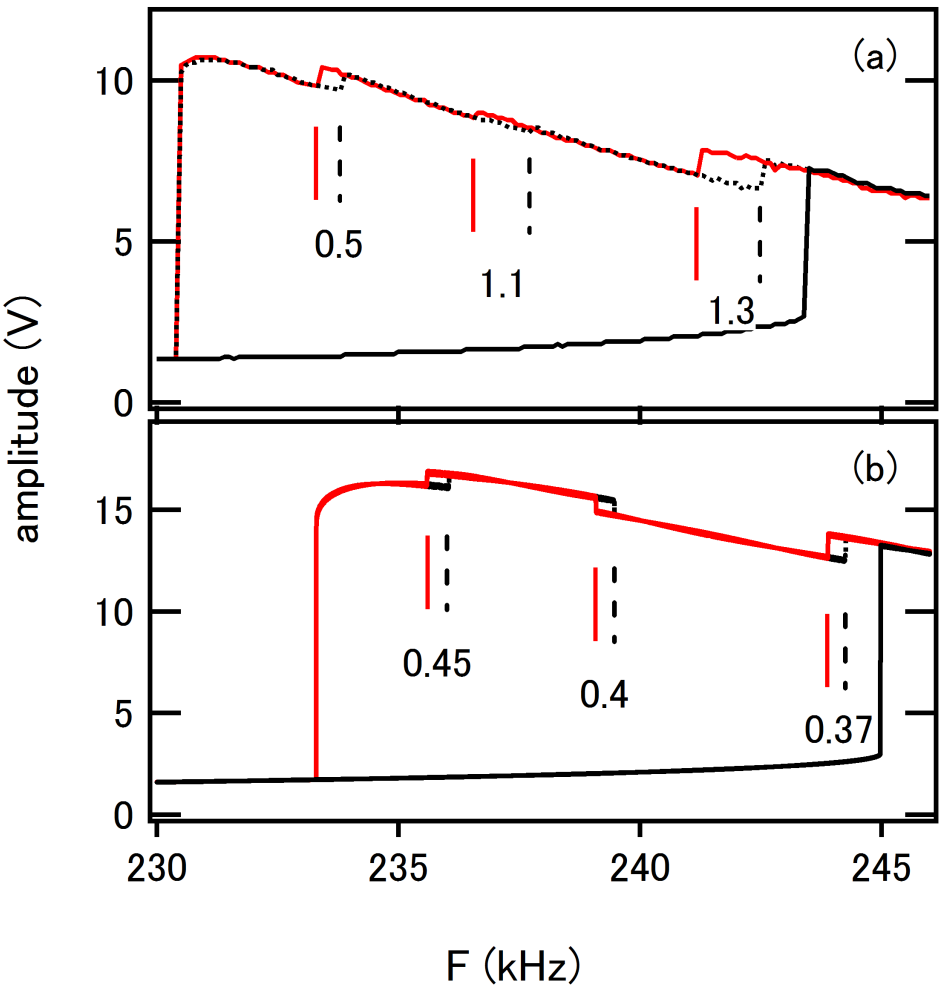

Figure 5.5: The maximum amplitude as a function of the driver frequency for measuring hysteresis. (a) Experimental results correspond to Fig. 3.4(d). (b) Simulation results adapted from Fig. 4.1(d). Vertical solid (dashed) lines indicate frequencies of step transitions for down (up) scanning case.

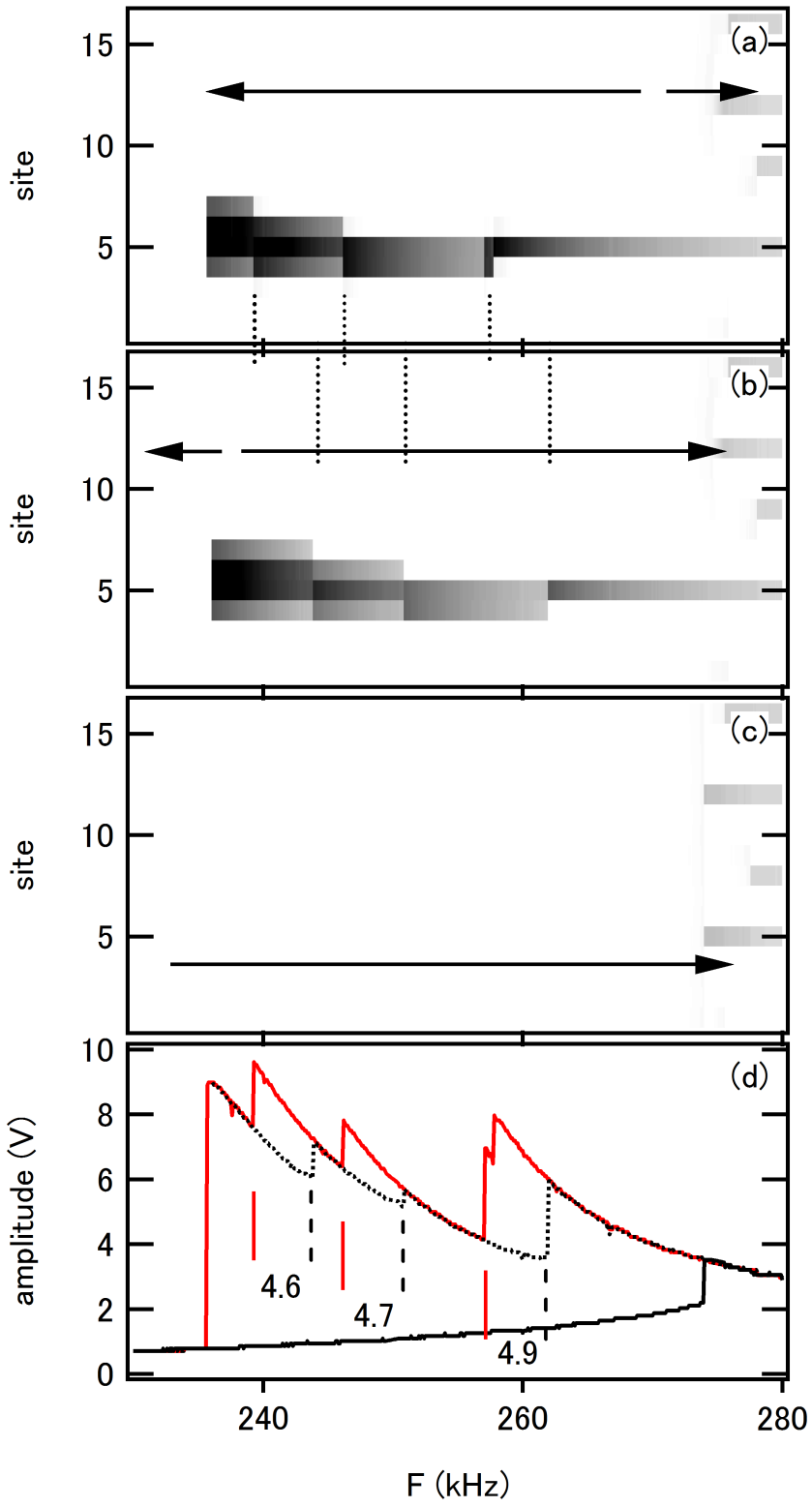
(a)
(b)
(c)
(d)
site
site
site
amplitude (V)
F (kHz)
15
10
5
10
8
6
4
2
0
240
260
280
4.6
4.7
4.9

Figure 5.6: Experimental amplitude plots as a function of the driver frequency. Darker represents a larger voltage. Arrows indicate frequency scanning directions. Vertical dashed lines denote frequencies of step transitions. (a) The driver frequency was up-scanned or down-scanned from an ILM state at a high frequency (270 kHz). (b) The frequency was scanned down or up from a low frequency (236 kHz). (c) Increasing the driver frequency from a low frequency below the stable ILM region. (d) The maximum amplitude as a function of the driver frequency. The upper red solid trace, the upper dashed trace and the lower trace correspond to Fig. 5.6(a), (b), and (c), respectively.

The observation of hysteresis between the step widening and narrowing transitions also gives us a hint to generate traveling ILMs in our nonlinear electrical lattice. It is known that ILMs must overcome a minimum barrier to propagate in the nonlinear lattice. [4, 5] When the barrier height is zero, ILMs can move freely. [1] It indicates that if the zero barrier height was located at the same frequency in step widening and narrowing transitions, moving ILMs can be generated in the nonlinear electrical lattice. In other words, the solution of hysteresis inside the stable ILM region is the key to generate traveling ILMs.

Back to our experiments, the solution of the stored charge in drain terminal becomes the key point to vanish hysteresis. A proposed avenue is that connects the drain and source terminal directly. However, this connection would decrease the nonlinearity as mentioned in Fig. 3.2 and the result is that the width of the ILM didnt change stepwise [6]. Therefore a new MOS-FET with larger nonlinearity than 2sj680 should be prepared in the nonlinear electrical lattice for solving the hysteresis problem.

References

[1] L. Hadžievski, A. Maluckov, M. Stepic, and D. Kip, *Phys. Rev. Lett.* **93**, 033901 (2004).

[2] M. Sato, S. Imai, N. Fujita, W. Shi, Y. Takao, Y. Sada, B. E. Hubbard, B. Ilic, and A. J. Sievers, *Phys. Rev. E* **87**, 012920 (2013).

[3] V. Hizhnyakov, A. Shelkan, M. Klopov, S. A. Kiselev, and A. J. Sievers, *Phys. Rev. B* **73**, 012920 (2006).

[4] R. Morandotti et al., *Phys. Rev. Lett.* **83**, 2726 (1999).

[5] Y. S. Kivshar and D. K. Campbell, *Phys. Rev. E* **48**, 3077 (1993).

[6] W. Shi, S. Shige, H. Hasebe, M. Sato, and A. J. Sievers, *Proceedings of "2013 International Symposium on Nonlinear Theory and its Applications"*, Santa Fe (2013).

Chapter 6

Summary

Step widening/narrowing of the ILM in a nonlinear electrical lattice with saturable nonlinearity has been observed in our experiments. This phenomenon is caused by the softening of the 1st-LLM frequency difference as a step transition is approached. The softening of the 1st-LLM, corresponding to the decreasing of the PN barrier height, leads to the interchange of stability between site-centered and bond-centered ILM locations. This is consistent with previous theoretical work [1].

The softening of the NF frequency difference gives rise to the lower fundamental transition observed at the lower edge of the stable ILM region. This transition is similar to the saddle-node bifurcation in the Duffing resonator. [2] The creation of new LLMs is attributed to additional degrees of freedom of the ILM, caused by the expansion of the ILM. The LLMs can be classified into odd and even symmetries in the terms of the vibrating shape and appear alternatively.

Hysteresis, caused by the stored charge in the drain terminal, has been observed both in the experiments and the simulations, indicating the possibility of different

mechanisms for down and up scans. It prevents a free traveling since even at a transition a barriers still remains. However, we have succeeded in decreasing the hysteresis by tuning the lattice. If the hysteresis becomes negligibly small, the ILM could run freely.

References

[1] L. Hadžievski, A. Maluckov, M. Stepic, and D. Kip, *Phys. Rev. Lett.* **93**, 033901 (2004).

[2] M. Sato, S. Imai, N. Fujita, W. Shi, Y. Takao, Y. Sada, B. E. Hubbard, B. Ilic, and A. J. Sievers, *Phys. Rev. E* **87**, 012920 (2013).